Electrostatic Control of Single InAs Quantum Dots using InP Nanotemplates

A THESIS

SUBMITTED TO THE FACULTY OF SCIENCE

IN PARTIAL FULFILLMENT OF THE REQUIREMENTS

FOR THE DEGREE OF

MASTER OF SCIENCE

IN THE DEPARTMENT OF PHYSICS

AT THE

UNIVERSITY OF OTTAWA

Ottawa, Canada, 2012

Electrostatic Control of Single InAs Quantum Dots using InP Nanotemplates

Ross Cheriton

February 2012

Contents

1 Introduction **3**

1.1 Outline of this Thesis 3

1.2 Introduction 3

1.3 Route to self-assembled quantum dots 5

1.4 Objective of this Thesis 10

2 Theory **12**

2.1 Introduction 12

2.2 Band structure 13

2.3 Density of states 14

2.4 Excitons 15

2.5 Three-dimensional confinement 16

2.6 Quantum dots 18

2.7 Dots in magnetic field 21

3 Experimental setup **23**

3.1 Chemical beam epitaxy 23

3.2 Optical spectroscopy 24

4 Quantum dot nanotemplates **29**

4.1 Introduction 29

4.2 Growth of self-assembled InAs quantum dots on InP nanotemplates . . 30

4.3 Photoluminescence of single InAs quantum dots on InP nanopyramids . 35

4.4 Chapter summary and comments 38

5 Electrostatic gating of InAs quantum dots **39**

5.1 Introduction 39

5.2 Fabrication of electrostatic gates 41

5.3 Bond pads and wire bonding 44

5.4 Exchange splitting 45

5.5 Vertical electric field 50

5.6 Lateral electric field 51

5.7 Quadrapole electric field 54

5.8 Chapter summary 56

6 Magnetophotoluminescence spectroscopy of single InAs/InP dots in pyramidal nanotemplates 58
6.1 Introduction 58
6.2 Magnetophotoluminescence spectroscopy of single InAs/InP dots 59
6.3 Excitonic g-factor and diamagnetic shift 64
6.4 Polarization-resolved spectroscopy 70
6.5 Chapter summary 71

7 Conclusions 72
7.1 Conclusions 72
7.2 Future work: Gated dots in photonic crystal cavities 73
7.3 Future work: Gated dots in magnetic fields 75
7.4 Statement of work 77

List of Figures

1.1 Plot of the attenuation of transmitted light through a single mode fibre as a function of wavelength. 9

2.1 Band structures of metals, semiconductors and insulators. 13
2.2 Schematic of the density of states distribution for three-dimensional, two-dimensional, one-dimensional and zero-dimensional structures. 15
2.3 Schematic of a particle in a box with length, width and height labeled as L_x, L_y and L_z, respectively. 17
2.4 TEM cross-section micrograph of a single InAs/GaAs self-assembled quantum dot 18
2.5 Distribution of electron and hole states shown grouped into shells for a lens-shaped quantum dot. 19
2.6 The electron and hole energy states of a lens-shaped quantum dot, along with a diagram of a lens-shaped quantum dot. 21

3.1 Schematics of the epitaxial growth processes involved in a) MOCVD, b) MBE and c) CBE 25
3.2 Schematic drawing of the photoluminescence spectroscopy setup used to optically characterize quantum dot samples. 26
3.3 Laboratory equipment used for photoluminescence spectroscopy. 27
3.4 Top-view of the optical spectroscopy setup used to study quantum dots. 28

4.1 A single etched square through the SiO_2(lighter), exposing the InP substrate(darker) below. 30
4.2 SEM micrographs of uncapped pyramids. 33
4.3 Photoluminescence spectra of single pyramids with decreasing side length. 34
4.4 Schematic of the growth process of the InP pyramidal nanotemplate. . 35
4.5 Photoluminescence of a single dot in a pyramid at low power. 36
4.6 Power spectrum of a single dot in a pyramid. 37
4.7 Single photoluminescence peak from a quantum dot. 38

5.1 The biexciton cascade for a quantum dot. 40
5.2 The pyramidal nanotemplate with metallic gates on the sides. 42
5.3 Quadrapole electric field as (a) a 3D surface plot and (b) a 2D colour map. The colour and height of the surface represents the electric field. . 43

5.4 IV curves of four functioning gates on the sidewalls of a pyramidal nanotemplate. 43
5.5 Picture of a sample in a chip mount. 45
5.6 Images of the gating configuration for a single pyramidal nanotemplate. 46
5.7 An SEM micrograph of a completely destroyed gated pyramid. 47
5.8 Schematic of the polarization optics used to isolate and identify the photoluminescence from each exciton transition. 48
5.9 Plot of the energy of photoluminescence peaks for the X^0, XX and X^{-1} states as a function of half-wave plate angle. 49
5.10 Cross-section schematic of the vertical gating configuration on a pyramidal nanotemplate. 50
5.11 Photoluminescence from a single dot as a function of voltage between the top gates and the back gate. 51
5.12 Schematic of the lateral gating configuration. 52
5.13 Photoluminescence spectra of a single dot as a function of lateral electric field intensity. 53
5.14 Emission peak energy as a function of wave plate angle for increasing lateral electric fields. 55
5.15 The reversal of the phase of the exchange splitting as a function of quadrapole field strength. 56

6.1 Photograph of the experimental apparatus for magnetophotoluminescence spectroscopy. 60
6.2 SEM micrographs of the dense array of pyramids and alignment ridges. 61
6.3 Schematic of the entire sample with a dense array of pyramids. 62
6.4 Schematic of the medium alignment structures of the sample. 63
6.5 Schematic of the dense array of pyramids and crosses. 64
6.6 Photoluminescence spectra as a function of magnetic field at low and high laser power. 65
6.7 Photoluminescence spectra of a single dot in a pyramid as a function of laser power. 66
6.8 Photoluminescence spectra as a function of magnetic field intensity at low and high laser power. 67
6.9 Exciton g-factor as a function of ground state emission energy. 68
6.10 Diamagnetic coefficient as function of the ground state emission energy of the X^0 and X^{-1} states. Error bars are too small and are not shown for clarity. 69
6.11 The g-factor of the X^0 and X^{-1} states plotted as a function of the diamagnetic coefficient. Error bars are too small and are not shown for clarity. 69
6.12 Polarization-resolved magnetophotoluminescence spectra of a single dot. 70

7.1 SEM image of a gated photonic crystal cavity. 75
7.2 Gated sample on a plastic spacer. 76

7.3 Optical micrograph of a gated sample beside a reference sample with alignment marks. 77

List of Tables

4.1 Step-by-step InP nanotemplate and InAs quantum dot growth procedure in the CBE chamber. 32

Acknowledgments

Nearing the end of my Master's program in Physics, I am humbled by the support from my friends, family, supervisor, co-workers and fellow students. There are not enough words in this Thesis to adequately describe how thankful I am to those who have helped and guided me throughout this adventure. I would like to thank my Thesis supervisor, Dr. Robin Williams, for his time and dedication to my education and development as a young scientist. With his door always being open to me, I have been very fortunate to be to learn his priceless lessons in critical thinking and quality work. Without his guidance, inspiration and demand for only the best science, I would not be the student I am today.

In my research, I am thankful to be surrounded by a dedicated and inspiring team of scientists with the Institute for Microstructural Sciences at NRC. I would like to thank Dr. Dan Dalacu for not only making the results in this Thesis possible, but always having the patience for my inexperienced self. His great experience and knowledge of the field has always been there for me countless times. I am blessed to work alongside Simon Frédérick, Khaled Mnaymneh, Philip Poole, Jacques Lefebrve, Vera Sazonova, Pawel Hawrylak, Marek Korkusinski, Geoff Aers, Joe McKee, Martha Tomlinson and Jean Lapointe and entire team of researchers at IMS for their wealth of knowledge and the incredible scientific environment they have created.

Next, I am grateful to my parents, Huda and Glenn, and my two sisters, Noor and Sherry, whose love and support has always been my motivation to accomplish anything in life. I am eternally thankful to be part of my family, who have always done so much for me and taught me the values I need to achieve my dreams. Thirdly, I would like to thank Trista Takacs and her parents for their support throughout my Master's studies. Trista's patience and understanding have inspired me during my studies, shaping my life for the better. Finally, I would like to thank the committee members for their astute comments and suggestions for revisions. Their keen perceptions have undoubtedly helped to maintain the highest scientific standards, allowing this thesis to be the best it can be.

Electrostatic Control of Single InAs Quantum Dots using InP Nanotemplates

by
Ross Cheriton
Master of Science
University of Ottawa
Supervisor: Professor Robin L. Williams

Abstract

This thesis focuses on pioneering a scalable route to fabricate quantum information devices based upon single InAs/InP quantum dots emitting in the telecommunications wavelength band around $\lambda = 1550$nm. Using metallic gates in combination with nanotemplate, site-selective epitaxy techniques, arrays of single quantum dots are produced and electrostatically tuned with a high degree of control over the electrical and optical properties of each individual quantum dot. Using metallic gates to apply local electric fields, the number of electrons within each quantum dot can be tuned and the nature of the optical recombination process controlled. Four electrostatic gates mounted along the sides of a square-based, pyramidal nanotemplate in combination with a flat metallic gate on the back of the InP substrate allow the application of electric fields in any direction across a single quantum dot.

Using lateral fields provided by the metallic gates on the sidewalls of the pyramid and a vertical electric field able to control the charge state of the quantum dot, the exchange splitting of the exciton, trion and biexciton are measured as a function of gate voltage. A quadrapole electric field configuration is predicted to symmetrize the product of electron and hole wavefunctions within the dot, producing two degenerate exciton states from the two possible optical decay pathways of the biexciton. Building upon these capabilities, the anisotropic exchange splitting between the exciton states within the biexciton cascade is shown to be reversibly flipped. We show direct control over the electron and hole wavefunction symmetry, thus enabling the entanglement of emitted photon pairs in asymmetric quantum dots.

Optical spectroscopy of single InAs/InP quantum dots atop pyramidal nanotemplates in magnetic fields up to 28T is used to examine the dispersion of the s, p and d shell states. The g-factor and diamagnetic shift of the exciton and charged exciton states from over thirty single quantum dots are calculated from the spectra. The g-factor shows a generally linear dependence on dot emission energy, in agreement with

previous work on this subject. A positive linear correlation between diamagnetic coefficient and g-factor is observed.

Chapter 1

Introduction

1.1 Outline of this Thesis

This thesis begins with an introduction to the field of quantum dots, giving an historical overview and discussing the main reasons for interest in quantum dot nanostructures. The theory behind quantum confinement effects in quantum dots is then presented in Chapter Two. To provide a physical perspective on the research, Chapter Three outlines the fabrication processes of the growth of InAs/InP quantum dots, the spectroscopic techniques and experimental apparatus used in their study. The design, fabrication and modification of the nanotemplate, and also photoluminescence spectroscopy of single InAs/InP quantum dots is shown in Chapter Four. Chapter Five focuses on the electrostatic gating of the nanotemplate through descriptions of lateral and vertical gating effects on the charge state, and measurements of the exchange splitting of the exciton, trion and biexciton as function of gate voltage. Chapter Six is an overview of the magnetospectroscopy of single dots in nanotemplates where the g-factor and diamagnetic coefficients are measured and their significance in this thesis is discussed.

1.2 Introduction

The science and technology of nanoscale structures has received much attention over the last decade. New research areas including carbon nanotubes, quantum dots and graphene amongst others, have led to developments such as ultralight electrical wires[1], quantum computation[2, 3] and devices with unprecedented electrical properties[4]. In the pursuit of applications such as these, novel effects made possible by the quantum mechanical properties of matter at the nanoscale have sparked interest in smaller and smaller structures[5]. In order to access these new quantum mechanical effects, particles must be confined to dimensions smaller than their de Broglie wavelength. The unique physics at the nanoscale has hinted at the potential to create devices which work faster, are more reliable or incorporate new functionalities.

A quantum dot can be thought of as any structure capable of complete, three-dimensional confinement of particles near the scale of their de Broglie wavelength. Realized in the solid-state, self-assembled quantum dots are typically semiconductor nano-crystals, comprising thousands or millions of atoms, surrounded by a crystalline semiconductor matrix with a larger band gap. The difference in band gap creates a potential well for electrons and holes confined within the quantum dot. In addition, quantum dots have been labeled as artificial atoms due to the discrete energy states they occupy in correspondence with real atoms. The energy of the photons emitted from the quantum dot following the annihilation of a trapped electron-hole pair is determined by the materials involved and the confinement dimensions of the quantum dot. Research has shown that the shape of the quantum dot plays an important role in the optoelectronic properties of these quasi-zero-dimensional structures[6].

Researchers have been able to fabricate quantum dots for about forty years. Presently, using modern molecular beam epitaxy(MBE) growth techniques, high quality epitaxial quantum dots can be reliably grown. Using photoluminescence(PL) spectroscopy, the discrete energy structure of these quantum dots can be characterized[7].

The ability to reliably fabricate quantum dots has led to an increased interest in possible applications, including solar cells[8], batteries[9], medical labeling[10], quantum computing[2], single photon sources[11, 12], lasers[13] and many other technologies. However, in order to develop these technologies, quantum dot research must shift from the characterization of their properties to the control of their properties for device applications. The difficulty in realizing these technologies in physical devices arises from the inherent randomness in the fabrication of quantum dots. The task of incorporating quantum dots into real-life devices requires the ability to engineer quantum dots for a specific emission wavelength, location, charge state etc. The simultaneous control of all such variables will enable routine demonstrations of photon antibunching and the generation of entangled photons from single quantum dots, which are fundamental requirements for optical quantum information devices.

At present, antibunching statistics and entanglement of emitted photons have been achieved using single quantum dots. As impressive as these accomplishments are, they are not without severe limitations. The single photon device[14] is not able to emit photons which have low attenuation in optical fibre. The device is also produced using techniques that are not scalable, due to the random nature of the quantum dot nucleation position and emission wavelength. The entanglement of photons from a single dot[15] has been demonstrated by introducing a large magnetic field or by selecting specific dots from a large collection; techniques which are not practical if one wishes to manufacture large numbers of sources. The inherent drawbacks of these proof-of-concept techniques must be overcome if large numbers of practical quantum information devices are to be produced.

This thesis describes a technique to control the position, size, shape and emission wavelength of single InAs/InP quantum dots emitting in the wavelength regime suitable for long-distance transmission of photons through optical fibre ($\tilde{1}$550nm)[16]. Locally positioned Schottky gates are used to reversibly control the charge state of individual dots and to apply lateral electric fields in the plane of dot growth. Control of the electron-hole confining potential is demonstrated using a quadrapole electric field applied using electrostatic gates localized at close proximity to a single dot. The effect of the quadrapole field on the exchange splitting between the two spin configurations of the neutral exciton is explored. Considering the pursuit of full control over a single quantum dot, this thesis addresses many of the issues hindering the incorporation of single quantum dots into future solid-state quantum information architectures.

1.3 Route to self-assembled quantum dots

The properties of bulk materials have been extensively studied and applied in solid-state devices for a considerable time. The discovery of quantum confinement effects has led to the birth of the field of nanotechnology, where the physics of low-dimensional structures can be used to improve the performance of solid-state devices.

The first examples of such structures were quasi-two-dimensional layers of atoms, where these atoms were epitaxially deposited to produce alternating layers of materials with differing properties. By tuning the thickness of these layers, the electronic and optical properties of the materials could be controlled. These stacks are called heterostructures. The properties of these structures were unlike those of any traditional bulk material. As the thickness of the layers approached the de Broglie wavelength of the electron, the electrons in the material begin to behave as if they were confined to a two-dimensional plane [17]. This type of confinement is called a quantum well, where the motion of the electron is quantized along one dimension. The density of electron states of a quantum well is quantized into steps, departing from the usual smooth distribution of states in bulk material. As the technology progressed, monolayer-precision control over the thickness of quantum wells became commonplace. As a result, a multitude of applications arose, from high performance lasers[18], low-noise electronics[19] and saturable absorbers[20], to doped quantum wells, where exotic quantum effects like the quantum Hall effect were discovered[21].

Confining a particle in two directions results in a one-dimensional structure called a quantum wire. Electrons in these wires would be free to travel along the length of wire but would be confined in directions transverse to the wire. For dimensions smaller than a few hundred nanometers, the electrical properties of these wires are heavily dependent on the confinement of the electrons. For example, the resistivity becomes quantized[22]. The two-dimensional confinement of wires introduces a semi-discrete density of states.

The study of quasi-zero-dimensional nanostructures diverged into separate fields, dictated by very different fabrication techniques. Beginning in the early 1980's, the first mention of quantum size effects in three-dimensionally confined structures arose from structures synthesized in colloidal solution[5]. Such structures were subsequently called "quantum dots" by Reed[23]. This type of fabrication procedure for quantum dots has been used to demonstrate precise control over nanocrystal size and correspondingly their emission wavelength[24]. Although the colloidal synthesis of quantum dots is relatively simple and the quantum dot ensemble can be tuned to emit at specific wavelength, accessing a single colloidal quantum dot for scalable quantum information processing has proven impractical.

An alternate type of quantum dot was formed from a doped quantum well by restricting the lateral dimensions using electrostatic gates. With the development of high quality doped quantum wells, it was found that by applying voltages to metallic gates positioned on top of a sample, electrons could be confined laterally in a vertically-confined electron gas[25]. This resulted in the creation of a potential minimum inside the electron gas, where one or more electrons could be trapped between the metallic gates. However, these quantum dots are only confined weakly in the lateral direction. In order to successfully trap electrons such small lateral confinement, temperatures on the order of millikelvins are required. The gating required in these quantum dots enables the manipulation of single electron spins as qubits. The difficulty in optically accessing the quantum dots and the ultra-low temperature requirement usually restricts the number of quantum dots, and hence the scalability. The study of these types of quantum dots is mainly limited to electronic transport measurements.

Early work with semiconductor quantum wells has shown that restricting the electronic degrees of freedom can reduce the threshold power of lasers. With this discovery began the progress and eventual success of quantum well structures for application in laser diodes, although the early fabrication procedures for constructing these types of devices were rather crude by modern standards. The development of molecular beam epitaxy(MBE) techniques enabled the growth of high quality semiconductor quantum wells and heterostructures[26]. This technique, which relies on epitaxially depositing thin layers of various semiconductor compounds, has led to the observation of different types of growth modes, from layer by layer two-dimensional growth, to three-dimensional growth of isolated semiconductor "islands", and a mode in between. Of particular interest here is the intermediate Stranski-Krastonov growth mode, named in reference to the early work of Ivan Stranski and Lyubomir Krastanov in 1939[27], where growth is initiated in a layer by layer manner but then quickly switches to fully three-dimensional growth of small, coherent, defect-free islands. These random islands in the deposited material were later recognized as structures that could serve as quantum dots.

The quantum dot islands produced in the Stranski-Krastonov growth mode are the result of a lattice mismatch between the deposited semiconductor material and the substrate. Following the initial few monolayers of growth (called the wetting layer), the system evolves towards a configuration that minimizes the total strain, producing isolated three-dimensional islands or quantum dots. These randomly distributed quantum dots typically grow to sizes of a few tens of nanometers in diameter, with thicknesses of about 3-5nm. The spontaneous nucleation of the islands formed during Stranski-Krastonov growth has led to them being labeled as "self-assembled" quantum dots. The islands are capable of full, three-dimensional confinement of electrons, holes and bound states of electron-hole pairs called "excitons"[28]. Lateral interface fluctuations in quantum wells have also been reported which also result in sharp excitonic emission lines indicative of quantum dot formation[29].

Optical spectroscopy of quantum dots grown using the Stranski-Krastonov growth mode has allowed the observation of photoluminescence from a large number(or ensemble) of quantum dots. Size variations between individual dots led to a range of possible emission wavelengths. The resulting spectroscopy of an ensemble of quantum dots produces a broad, Gaussian-like emission peak representing the distribution of quantum dots sizes. This broadening is called inhomogeneous broadening. To study single quantum dots, one typically fabricates a sample with a low density of dots[30] and optically excites only a single dot using a method called microphotoluminescence (or μPL)[31]. In one version of this technique, a metallic mask is deposited across the sample containing small holes which may align with individual dot positions. The spectroscopic isolation of quantum dots allows one to measure the linewidth of the emission peak and hence the radiative lifetime of the exciton, providing direct evidence of the atomic-like properties of individual quantum dots.

Although the optical properties of single quantum dots can be studied, no practical device that uses a single quantum dot should rely on these stochastic selection procedures. Nevertheless, the properties of most single quantum dots continue to be studied using such a procedure, since a way to deterministically control the location of individual dots is not generally available.

The vast majority of self-assembled quantum dots are formed using indium arsenide (InAs) as the dot material and Gallium Arsenide (GaAs) as the barrier material. The lattice constant mismatch between these two materials is about 6.7%, creating a large strain field at the interface[32]. This system yields quantum dots with ground state emission wavelengths from 800nm to 1.3μm, with a moderate inhomogeneous broadening of the quantum dot ensemble.

In the early stages of quantum dot fabrication, the observation of optically bright quantum dots was rare. Smaller quantum dots resulted in poor photoluminescence due to the longer relaxation lifetimes[33]. There was subsequently work to circumvent this issue[34].

Modern, high quality InAs/GaAs dots are limited to wavelengths smaller than approximately 1μm, which are unsuitable for guided transmission through telecommunications optical fibre. The ideal quantum dot system would emit photons with wavelengths around 1.55μm, where these photons pass through pure silica optical fibre with the lowest attenuation, approximately 0.2dB/km, as shown in Figure 1.1. Strategies involving a more complex use of combinations of materials[35], such as InGaAs for the dot material[36, 37], aimed to reduce the strain between the two materials[38]. The resulting photoluminescence was shifted to wavelengths around 1.3μm which approached the limit of what is possible using GaAs.

An alternate quantum dot system uses InAs quantum dots surrounded by InP. This system was first successfully introduced by R. Notzel *et al.* in 1995, despite poorer dot quality[39]. The lattice constant mismatch between these two materials is about 3%. The reduced strain between the two lattices allowed larger dots to form, resulting in quantum dots that emit photons with wavelength around 1.5μm, suitable for transmission through optical fibre[40, 41]. A property of InAs/InP quantum dots is the larger inhomogeneous broadening of the dot ensemble. The reduced strain allows for a larger size distribution of quantum dots.

Spatial isolation of single dots has proved to be difficult with InAs/InP materials, since the reduction of fluxes used with InAs/GaAs dots to produce a low dot density does not translate well to the InAs/InP system. Growth methods utilizing patterned

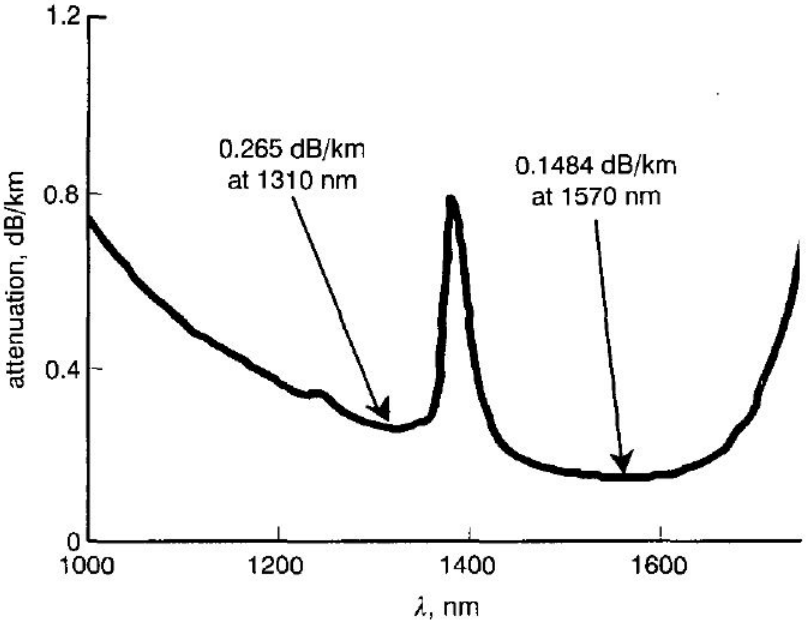

Figure 1.1: Plot of the attenuation of transmitted light through a single mode fibre as a function of wavelength. The wavelength which experiences the best transmission is 1500-1600nm, which coincides with the emission wavelength of InAs/InP quantum dot systems[44].

nanostructures, or microphotoluminescence techniques were developed to achieve dot isolation[42]. Other techniques using laser-induced diffusion in a quantum well were shown to produce quantum dots[43], but with a dot quality that did not match that of epitaxially-grown quantum dots.

InAs/GaAs quantum dots remain the most popular quantum dots for fundamental studies, since the fabrication procedures for InAs/GaAs dots are more mature than those for InAs/InP quantum dots, whilst the performance of optical detectors in the wavelength region below 1μm is far superior to those around 1.55μm. The silicon-based detectors which work below 1μm wavelength have lower noise figures than the InGaAs detectors typically used for detection of the longer wavelength photons emitted from InAs/InP quantum dots. It has required many years of work to produce high signal-to-noise optical spectra for InAs/InP quantum dots[45].

Today, the standard procedures used for the fabrication of quantum dots still yield quantum dots of varying size, position, charge state, brightness and shape. Attempts to control these quantities have had limited success. Previous work on isolating a single dot was done by etching a hole in a dielectric mask with a width on the order of a few tens of nanometers such that only a single quantum dot could grow in the opening.

The resulting quantum dots were not of the quality of those on planar substrates. The reason for this is the poor quality of the exposed GaAs substrate as a result of oxidation leading to the creation of surface states which broadened emission linewidths[46].

Nevertheless, the technique of microphotoluminescence allowed the study of single quantum dots on planar substrates, which was not possible with conventional spectroscopy. The proof of three-dimensional confinement in solid state systems generated a great deal of interest in quantum dots as artificial atoms. The study of single quantum dots enabled physicists to access fundamental quantum mechanical phenomena previously observed in atomic physics. Quantum information processing using solid-state architectures avoids the need for sophisticated cooling and atomic trapping equipment while having the potential for the scalability and practicality of devices.

For applications in optical quantum information processing, a scalable route to a device incorporating a single quantum dot coupled to the photonic mode of an optical cavity and emitting close to $\lambda = 1.55\mu$m is of great interest. For entangled photon emission, the electron-hole exchange splitting of the neutral exciton transition in this coupled dot-cavity system must be tuned to zero[15]. The work in this thesis addresses this latter goal through experiments to isolate and electrostatically gate a single InAs/InP dot.

With the use of pre-patterned substrates, the development of nanotemplate fabrication for high-quality quantum dot growth is a major theme in this thesis. Previous work [47, 48] has led to improvements such as optimal single dot isolation, gating of a single dot and other nanotemplate structures. The conclusion of this development results in a vertically and laterally gated single quantum dot with precisely controlled physical properties. This technology has focused on using this nanotemplate architecture to overcome the limitations of the ubiquitous quantum dot ensemble which faces inevitable challenges in scalability.

1.4 Objective of this Thesis

The primary goal of this thesis is to further develop the ability to electrostatically control a single InAs/InP quantum dot and to ultimately control the anisotropy of the single quantum dot confining potential in a manner that will permit on-demand entangled photon pair generation. The use of a quadrapole electric field configuration is explored as a method for controlling the symmetry of the quantum dot confining potential and hence control the degeneracy of the two possible spin configurations of the neutral exciton. The InAs/InP quantum dot system used in the present work is fully consistent with photon emission at wavelengths around $\lambda = 1.55\mu$m, suitable for transmission in telecommunications optical fiber. This benefit, along with the control over the dot isolation and positioning of single quantum dots, results in a very promising candidate as a fundamental building block for a scalable quantum dot device.

Other goals of this thesis are to build on the techniques of single quantum dot isolation, local electric fields and external magnetic fields to study the charge states of quantum dots. The charging spectra of single quantum dots are studied in detail, using lateral and vertical fields to charge a single quantum dot. Magnetic fields are used to further probe single dots in pyramidal nanotemplates. The g-factor and diamagnetic shifts of the exciton, trion and biexciton provide insight into the fine structure, physical symmetry and dipole moments of single dots.

As a whole, this thesis advances research on InAs/InP quantum dots from studying their random individual properties to engineering single quantum dots with a high degree of control. This control over quantum dot parameters is necessary to take the next step towards the scalability and application of devices for quantum information processing.

Chapter 2

Theory

2.1 Introduction

The optical and electronic properties of semiconductor quantum dots can be understood through the application of quantum mechanical theory to spatially-confined, solid-state structures comprising large numbers of atoms and containing small numbers of trapped electrons and holes. Since one of the primary characteristics of a quantum dot is its extremely small scale, the quantum confinement of particles is central to the scientific interest in these structures. Due to the complexity of solid state systems, many approximations must be made in order to develop a theory that even qualitatively describes the behaviour of single quantum dots. The $k \cdot p$ theory, which uses effective mass approximations, ignores atomistic effects and derives the single-particle states from a knowledge of the semiconductor band structure around the band edge. This methodology works reasonably well for InAs dots given some effective parameters. Tight-binding methods have been developed that can derive some of the parameters required as inputs for the $k \cdot p$ theory and can account for effects such as strain and dot/barrier interfaces without the complexities of first-principles methods[49].

This chapter presents a brief overview of the theory of band structure and optical excitations in the solid state environment. A simple particle-in-a-box model is described and the $k \cdot p$ theory is outlined for a single hole confined within a dot. The calculations of the g-factor and the diamagnetic coefficient from the magnetospectroscopy of single quantum dots are described.

2.2 Band structure

In bulk semiconductors, the large number of atoms occupying a three-dimensional crystalline lattice produces a set of continuous bands that correspond to allowed electron energies within the lattice. There is a range of energies where electronic states are forbidden, corresponding to a gap in the energy band structure. In typical, non-degenerate semiconductors, the Fermi level will lie close to the middle of the band gap, below the conduction band and above the valence band. At a temperature of absolute zero, electrons will fully occupy the valence band and the conduction band will be empty. An external excitation, such as an incident photon, can excite an electron from the valence band to the conduction band. A schematic diagram of the band structure in metals, semiconductors and insulators is given in Figure 2.1.

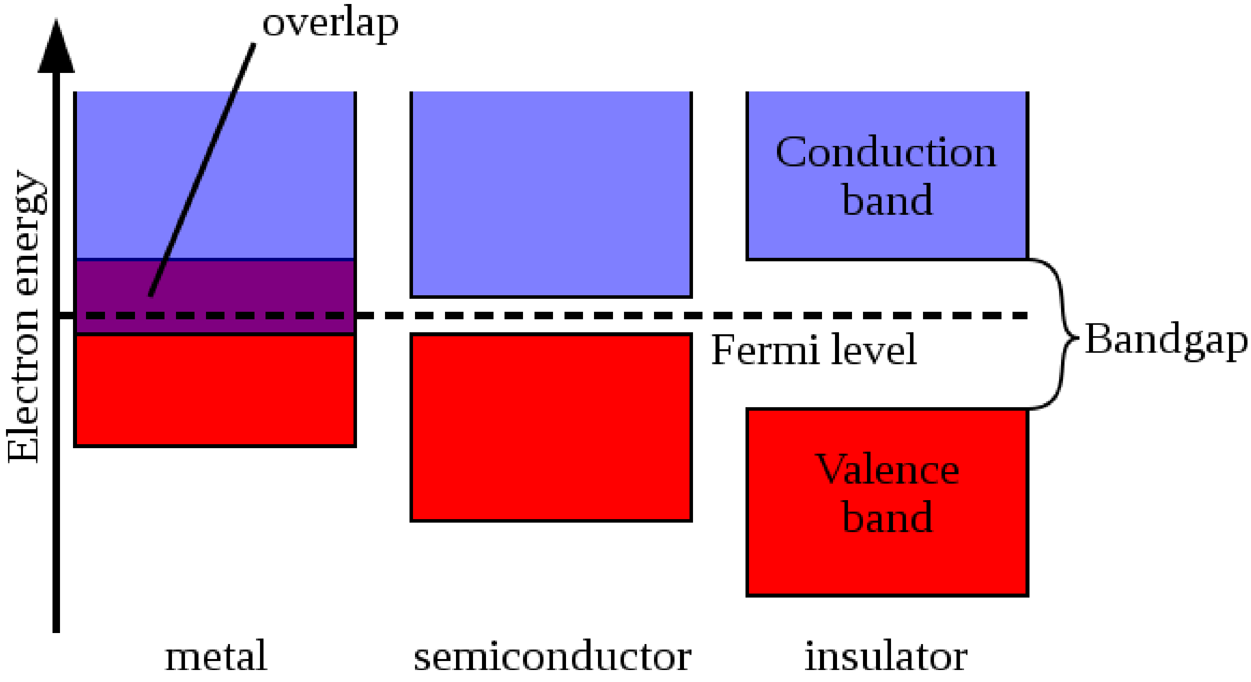

Figure 2.1: In a metal, the Fermi level lies within a band of allowed states. In a semiconductor, the Fermi level lies within a sufficiently narrow gap, typically of the order of 1eV. For semiconductors, thermal excitation of electrons from the valence band to the conduction band is possible at room temperature. In an insulator, the Fermi level again lies within the gap, but the gap is large enough such that any excitation of an electron to the conduction band is negligible at ordinary temperatures.

The research presented in this thesis focuses on the properties of semiconductors, as opposed to metals or insulators. The small band gap of semiconductors allows thermal (by phonons) or optical (by photons) excitation of carriers from the valence band to the conduction band.

2.3 Density of states

The density of states can be defined as the number of states per unit of energy. In a bulk semiconductor, an electron can exist in one of a continuum of states. One can calculate the density of states in bulk by finding the number of energy states that exist per spherical shell in k-space, where k is the wave vector of the freely propagating electron. If motion in one of the three dimensions is restricted to a length scale on the order of the de Broglie wavelength of the electron, one of the degrees of freedom is removed and the density of states changes dramatically.

For a bulk semiconductor, the density of states, $\rho_{3D}(E)$, can be written as

$$\rho_{3D}(E) = \frac{1}{2\pi^2\hbar^3}\sqrt{(2m^*)^3(E - E_{pot})}, \tag{2.1}$$

Where m^* is the effective mass and E_{pot} is the energy at the bottom of the band. For a quantum well, or two-dimensional semiconductor, the allowed k-states are restricted to a set of circular disks, giving a step-like density of states $\rho_{2D}(E)$,

$$\rho_{2D}(E) = \frac{m^*}{\pi\hbar^2 L_z}\sum_n H[(E - E_n)]. \tag{2.2}$$

Where L_z is the confinement length, H is the Heaviside step function, and E_n define the energies of the step edges. Restricting a second dimension defines a one-dimensional quantum wire with a semi-discrete density of states $\rho_{1D}(E)$,

$$\rho_{1D}(E) = \frac{\sqrt{2m^*}}{\pi\hbar L_y L_z}\sum_n \left(d\frac{H[E - E_m - E_n]}{\sqrt{E - E_m - E_n}}\right), \tag{2.3}$$

where L_y, L_z define the two confinement lengths, d is the degeneracy and E_m, E_n correspond to energy scales along the two confinement directions.

Fully-confined, zero-dimensional structures such as quantum dots produce a discrete, delta function-like density of states $\rho_{0D}(E)$,

$$\rho_{0D}(E) = \frac{1}{L_x L_y L_z}\sum_n \delta[E - E_l - E_m - E_n] \tag{2.4}$$

Where the additional confinement length is L_x, δ is the Dirac delta function and

E_l is the additional energy scale. Plotting the density of states versus energy, we can observe distinct qualitative differences between each type of structure, as shown in Figure 2.2.

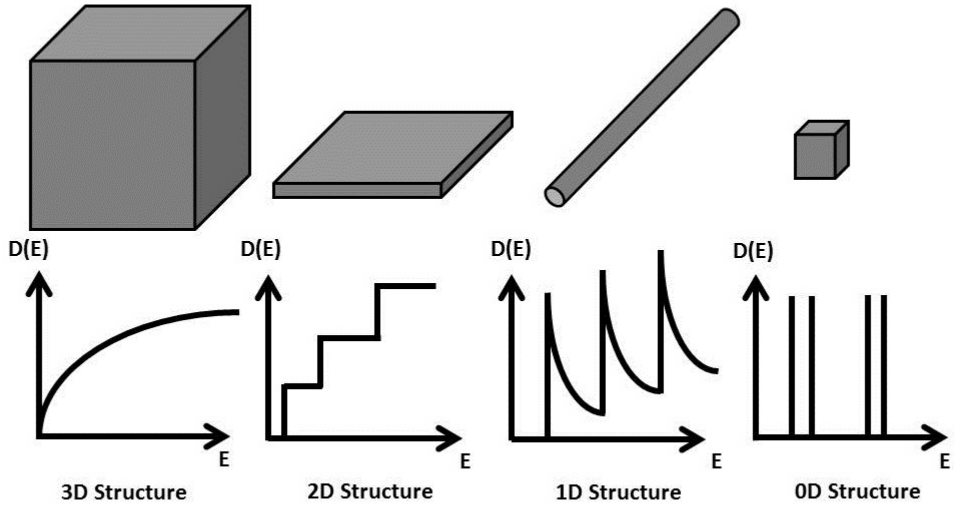

Figure 2.2: Schematic of the density of states distribution for three-dimensional, two-dimensional, one-dimensional and zero-dimensional structures, respectively. As quantum dots are quasi-zero-dimensional structures, their density of states is discrete.

2.4 Excitons

The promotion of an electron from the valence band to the conduction band in an undoped semiconductor necessarily leaves behind a "hole" in the otherwise full valence band. This hole can be described as a particle with an equal but opposite charge to that of the electron. The Coulomb attraction between the excited electron and hole gives rise to a bound state of the two particle system known as an exciton. The exciton, a quasi-particle, may move through the semiconductor until the electron is able to recombine with the hole, returning to the valence band and possibly resulting in the emission of a photon with an energy equal to the difference between the excited and ground state energies. In high quality, direct band gap semiconductors, the photon emission process can dominate at low temperatures, whilst at higher temperatures non-radiative processes compete.

There are two types of excitons: Frenkel excitons exist within materials of low dielectric constant, having large binding energies and sizes on the order of the unit cell dimension, whilst Wannier-Mott excitons exist within semiconductors of larger dielectric constant. Wannier-Mott excitons are weakly bound and have a size spanning many unit cells of the semiconductor. In self-assembled quantum dots, we encounter Wannier-Mott excitons due to the large dielectric constants of InP and InAs.

It is possible, with sufficient excitation from a laser, to create many excitons confined within a single dot. These multi-exciton complexes will themselves form bound states, the simplest of which is the biexciton, consisting of two excitons in the same dot. The biexciton state has a binding energy typically on the order of a few meV, and thus is usually spectrally distinguishable from the single exciton transition. Similar multi-exciton complexes can be formed with three or more excitons.

The presence of extra, uncompensated electrons or holes allows other, distinct states to occur. If an extra electron or hole is present within the dot during the recombination of an exciton, the emitted photon will be spectrally distinct from a photon emitted by the exciton alone. Many different charge states can exist with additional extra electrons or holes in the dot. For simplicity, excitons are labeled as X^0, biexcitons as XX, and charged excitons as X^{-1},X^{-2}...etc. or X^{+1}, X^{+2}...etc.

2.5 Three-dimensional confinement

To obtain some insight into the electronic structure of quantum dots, one can take the simplest "particle-in-a-box" model, as described in Figure 2.3. Beginning with the one-dimensional Schrödinger equation, we have

$$-\frac{\hbar^2}{2m^*}\left(\frac{\partial^2}{\partial x^2}\right)\psi(x)+V(x)\psi(x)=E\psi(x), \tag{2.5}$$

where m^* is the effective mass of the particle, $V(x)$ is the potential, $\psi(x)$ is the wavefunction of the electron in one dimension and E is the eigenenergy.

The solutions to this equation can be written as,

$$\psi(x)=A\sin(kx)+B\cos(kx) \tag{2.6}$$

Where A and B are constants chosen to satisfy the boundary and normalization conditions on the wavefunction. If the particle is strictly confined to a box of length L_x, we have

$$\psi_x(0)=0, \psi_x(L_x)=0 \tag{2.7}$$

such that,

$$\psi = A \cdot \sin(kx) \tag{2.8}$$

and

$$E = \frac{\hbar^2 k^2}{2m^*}. \tag{2.9}$$

From our second boundary condition, $\sin(k(L_x)) = 0$, we require $kL_x = n\pi$, where n is any integer. Solving for k and substituting we obtain,

$$E = \frac{\hbar^2}{2m^*}\left(\frac{\pi^2 n^2}{L_x^2}\right). \tag{2.10}$$

Extending the box to three dimensions and using the same reasoning, we arrive at the quantized energy states of a particle in a three-dimensional box,

$$E = \frac{\hbar^2}{2m^*}\left(\frac{{n_x}^2\pi^2}{{L_x}^2} + \frac{{n_y}^2\pi^2}{{L_y}^2} + \frac{{n_z}^2\pi^2}{{L_z}^2}\right), \tag{2.11}$$

where $n_x, n_y, n_z = 1, 2, 3$...etc.

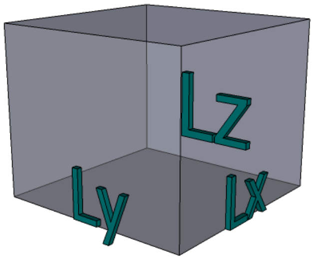

Figure 2.3: Schematic of a particle in a box with length, width and height labeled as L_x, L_y and L_z, respectively.

These discrete energy states result from the finite size of the box. As the size of the box is increased from the nanoscale towards macroscopic dimensions, the discrete energy states merge to form a continuum of states. The discrete distribution of energy states in quantum dots is due to this three-dimensional confinement of electrons and holes.

2.6 Quantum dots

In order to promote efficient electron-hole radiative recombination, spatial confinement is beneficial. Although instructive, the particle-in-a-box description of confinement within a quantum dot is not accurate. In addition to the complexities introduced by quantum dot alloy composition and strain, real dots can have various shapes similar to a lens, dome, disk or pyramid. A transmission electron micrograph of the cross-section of a single InAs/GaAs quantum dot is shown in Figure 2.4 (InAs/InP quantum dots are much flatter but have a similar shape). The states of real quantum dots are grouped into shells, much like atoms. The *s*, *p* and *d*-shells of a lens-shaped quantum dot are shown in Figure 2.5.

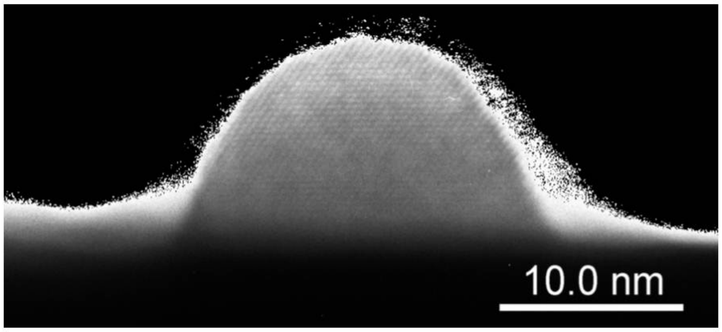

Figure 2.4: TEM cross-section micrograph of a single InAs/GaAs self-assembled quantum dot [50]. This is not an image of the type of dots studied in this Thesis. The dots in pyramidal nanotemplates do have the same shape, but are much flatter due to lower strain and lattice mismatch between InAs and InP. This image is shown to provide a qualitative, visual description of a typical self-assembled dot.

A relatively simple way to calculate the single-particle states is based on $k \cdot p$ perturbation theory within the effective mass approximation. The 4×4 Luttinger-Kohn Hamiltonian describes the energy states of a single hole close to the valence band maximum, including light holes, heavy holes and their mixing. Approximating the electronic states is simpler as it only requires the consideration of the conduction band states. This model can approximate the discrete energy distribution of dots in a quantum dot better than the particle-in-a-box model. The z direction is defined as the growth axis of the

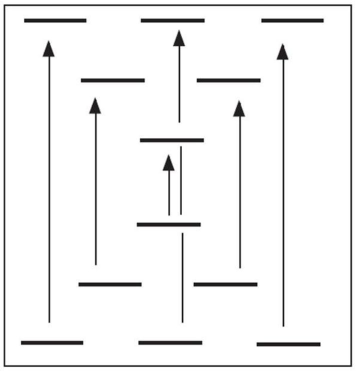

Figure 2.5: Distribution of electron and hole states shown grouped into shells for a lens-shaped quantum dot.

dot. The Luttinger-Kohn Hamiltonian has the form

$$\hat{H} = \begin{pmatrix} P_+ & R & -S & 0 \\ R^* & P_- & 0 & S \\ -S^* & 0 & P_- & R \\ 0 & S^* & R^* & P_+ \end{pmatrix}, \tag{2.12}$$

where the "$*$" represents the complex conjugate of an operator.

In the absence of applied electric and magnetic fields, the operators P_+, P_-, R and S are written as

$$P_+ = \frac{\hbar^2}{2m_0}\left[(\gamma_1 - 2\gamma_2){k_z}^2 + (\gamma_1 + \gamma_2)\hat{\mathbf{k_p}}^2\right], \tag{2.13}$$

$$P_- = \frac{\hbar^2}{2m_0}\left[(\gamma_1 + 2\gamma_2){k_z}^2 + (\gamma_1 - \gamma_2)\hat{\mathbf{k_p}}^2\right], \tag{2.14}$$

$$R = \frac{\hbar^2}{2m_0}\gamma_{23}\hat{\mathbf{k}_-}^2, \tag{2.15}$$

$$S = \frac{\hbar^2}{2m_0}(2\sqrt{3})\gamma_3\hat{\mathbf{k}_-}\hat{\mathbf{k_z}}, \tag{2.16}$$

where

$$\hat{\mathbf{k_x}} = -i\frac{\partial}{\partial x} \tag{2.17}$$

$$\hat{\mathbf{k_y}} = -i\frac{\partial}{\partial y} \tag{2.18}$$

$$\hat{\mathbf{k_z}} = -i\frac{\partial}{\partial z} \tag{2.19}$$

$$\hat{\mathbf{k_-}} = \hat{\mathbf{k_x}} - i\hat{\mathbf{k_y}} \tag{2.20}$$

$$\hat{\mathbf{k_p}}^2 = \hat{\mathbf{k_x}}^2 + \hat{\mathbf{k_y}}^2 \tag{2.21}$$

$$\gamma_{23} = \frac{\gamma_2 + \gamma_3}{2}. \tag{2.22}$$

The modeling of a charged particle in an electromagnetic field is achieved through the addition of the electromagnetic terms derived from Lagrangian mechanics. The Hamiltonian becomes

$$\hat{H} = \begin{pmatrix} P_+ & R & -S & 0 \\ R^* & P_- & 0 & S \\ -S* & 0 & P_- & R \\ 0 & S^* & R^* & P_+ \end{pmatrix} + \frac{(\mathbf{p} - e\mathbf{A})^2}{2m^*} + e\Phi, \tag{2.23}$$

where e represents the elementary charge, $\mathbf{A}$ is the vector(magnetic) potential, $\mathbf{p}$ is the momentum, and Φ is the scalar(electric) potential.

With a disk-like confining potential, the Hamiltonian can be expressed as

$$\hat{H} = \hat{H_{LK}} + V(\rho, z). \tag{2.24}$$

where ρ is the radial coordinate and the walls of the disk are assumed to be infinitely high for the case of strong hole confinement in dots. In this case, the radial wavefunctions are cylindrical Bessel functions and the vertical wavefunctions are simply those of an infinite square well, identical to those of the particle-in-a-box. In the same way the wavefunctions of the infinite well alternate in parity, the vertical component of the eigenstates show distinct parity in the form of Luttinger spinors. The Hamiltonian is diagonalized and the energy spectrum shows a series of distinct shells, as can be seen in Figure 2.6. Other dot geometries result in qualitatively similar shell structures.

Using $k \cdot p$ theory, accurate calculations of exciton states and wavefunctions in real quantum dots can be done with only a few effective material parameters. Much like in real dots, the theory describes the presence of distinct shells of states.

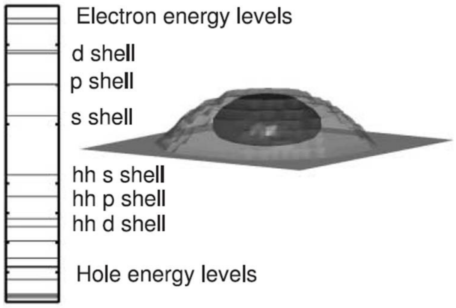

Figure 2.6: The electron and hole energy states of a lens-shaped quantum dot, along with a diagram of a lens-shaped quantum dot showing a 98% isosurface of the s-state of the electron[51].

2.7 Dots in magnetic field

We know from undergraduate physics that each atomic energy state is doubly degenerate in zero magnetic field as the result of the two possible spin configurations of the electron. In a quantum dot, the situation is completely analogous. Fundamentally, this degeneracy arises from the time reversal symmetry in the absence of a magnetic field, the so-called Kramers degeneracy theorem. In the presence of a magnetic field, the dispersion of the exciton states can be expressed as,

$$E_{\pm} = E_0 \pm g_{ex}\mu_B B + \gamma_D B^2, \tag{2.25}$$

where g_{ex} is the exciton g-factor, μ_B is the Bohr magneton, B is the magnitude of the magnetic field and γ_D is the diamagnetic coefficient.

The applied magnetic field interacts with the spin of particles and breaks the spin-degeneracy of the states. The dispersion of the two states is a combination of a linear and a quadratic effect.

The g-factor including the total angular momentum of the electron(spin and orbital angular momentum), also known as the Landé g-factor, is a measure of the linear splitting of the two states. The g-factor is a dimensionless quantity which describes the strength of the coupling between total angular momentum of a particle and the magnetic field. The total magnetic moment of the exciton is defined below:

$$\boldsymbol{\mu_{ex}} = g_{ex}\mu_B \frac{\mathbf{J}}{\hbar}, \tag{2.26}$$

where $\boldsymbol{\mu}$ is the magnetic moment and $\mathbf{J}$ is the total angular momentum.

This g-factor is experimentally measured using the relation

$$g_{ex} = \frac{E(\omega_+) - E(\omega_-)}{\mu_B B}, \tag{2.27}$$

where $E_(\omega_+)$ and $E_(\omega_-)$ are the higher and lower states split by the magnetic field, respectively.

If Equation 2.25 is solved for γ_D while using the average energy of the two spin states, we obtain

$$\gamma_D = \frac{E_{av} - E_0}{B^2} \tag{2.28}$$

where $E_{av} = \frac{E_(\omega_+)+E_(\omega_-)}{2}$.

The diamagnetic shift is the quadratic component of the dispersion of the states in the presence of a magnetic field. The diamagnetic coefficient is calculated using Equation 2.28 once the g-factor is measured.

Chapter 3

Experimental setup

3.1 Chemical beam epitaxy

For nanostructures such as the InAs/InP quantum dots studied here, the ratio of surface area to volume is large. One consequence of this is that the behaviour of individual dots is particularly sensitive to defects or contamination at or near the quantum dot surface. To achieve high optical quality, well-controlled, InAs/InP quantum dots it is therefore necessary to prepare them using a technique that avoids, as much as possible, the incorporation of potential contaminants. For the preparation of these semiconductor structures, a number of epitaxial growth techniques are available, including Molecular Beam Epitaxy (MBE), Molecular Organic Chemical Vapor Deposition (MOCVD) and Chemical Beam Epitaxy (CBE). Each of these techniques can be used to grow high quality material, but they differ in the details of the mechanism used for growth. MBE is an ultra-high vacuum deposition technique (10^{-11} Torr base pressure, 10^{-8} Torr during growth) typically employing elemental solid source starting materials (indium, arsenic, gallium, phosphorous etc.). Source materials are heated to produce elemental beams that are then directed onto a heated semiconductor substrate to initiate growth. MOCVD is a higher pressure growth technique ($10-1000$ Torr), where saturated vapors of the source gases, typically in hydrogen carrier gas, flow across the heated substrate. MOCVD is the growth technique of choice in many industrial applications, as the material quality can be extremely high and the technique lends itself to multi-wafer, high throughput production.

The InAs/InP quantum dot structures studied in this thesis were produced by CBE, using procedures developed at the National Research Council of Canada. CBE is an ultra-high vacuum growth technique similar to MBE, but with gaseous sources (Arsine, Phosphine, Trimethylindium, Triethylgallium etc.). A schematic diagram showing the essential features of MBE, CBE and MOCVD is given below in Figure 3.1. During growth, the CBE chamber is maintained at a pressure below 10^{-8} Torr using a combination of turbo-molecular and cryo-pumps, while the InP substrate, mounted in a molybdenum sample holder, is kept at a temperature close to 500°C. The entire growth environment is surrounded by a hollow-walled stainless steel shroud containing liquid nitrogen, as a further means for contamination control and cryo-pumping. A unique feature of the CBE system used to prepare the samples studied here is that the system incorporates an embedded scanning electron microscope, so that nanostructures can be viewed in-situ and monitored in real-time during growth.

A particular feature of the CBE growth technique that is exploited for the present work is that of site-selective epitaxy. Prior to growth, the InP substrates are coated with a thin layer (typically 20nm) of SiO_2 and small windows are opened in the dielectric using electron-beam lithography to expose the underlying substrate. CBE growth of InP on such a substrate produces growth only on the regions of exposed substrate, since the chemical cracking of the source materials requires a heated substrate to act as a catalyst. No deposition occurs on the SiO_2. Growth of InP on the regions of exposed substrate can be controlled through the size, orientation and shape of the windows, to produce square- or rectangular-based pyramidal InP templates that can then accommodate InAs quantum dots at their apex. In this manner, the nucleation position of individual InAs/InP quantum dots can be controlled with high precision.

3.2 Optical spectroscopy

To facilitate the measurement of photoluminescence from individual quantum dots, an experimental configuration was employed that allowed white-light imaging of the sample while inside a continuous flow, liquid helium cryostat at low temperature. The sample was optically excited using the 632.8 nm line from a helium-neon laser source that was split using a beam splitter to measure the incident laser power and focused onto the sample using a long working distance Mitutoyo® microscope objective. With a magnification of 20, the excitation spot size at the sample surface was approximately 5μm in diameter.

Quantum dot emission was collected back through the microscope objective and directed onto a cold mirror. The infrared wavelengths were then passed through a long-pass filter to block scattered laser light and focused onto the slit of a 0.25m, single-pass grating spectrometer for dispersion, before being detected by a liquid nitrogen-cooled InGaAs diode array in the focal plane. For low-resolution spectroscopy, a 149-

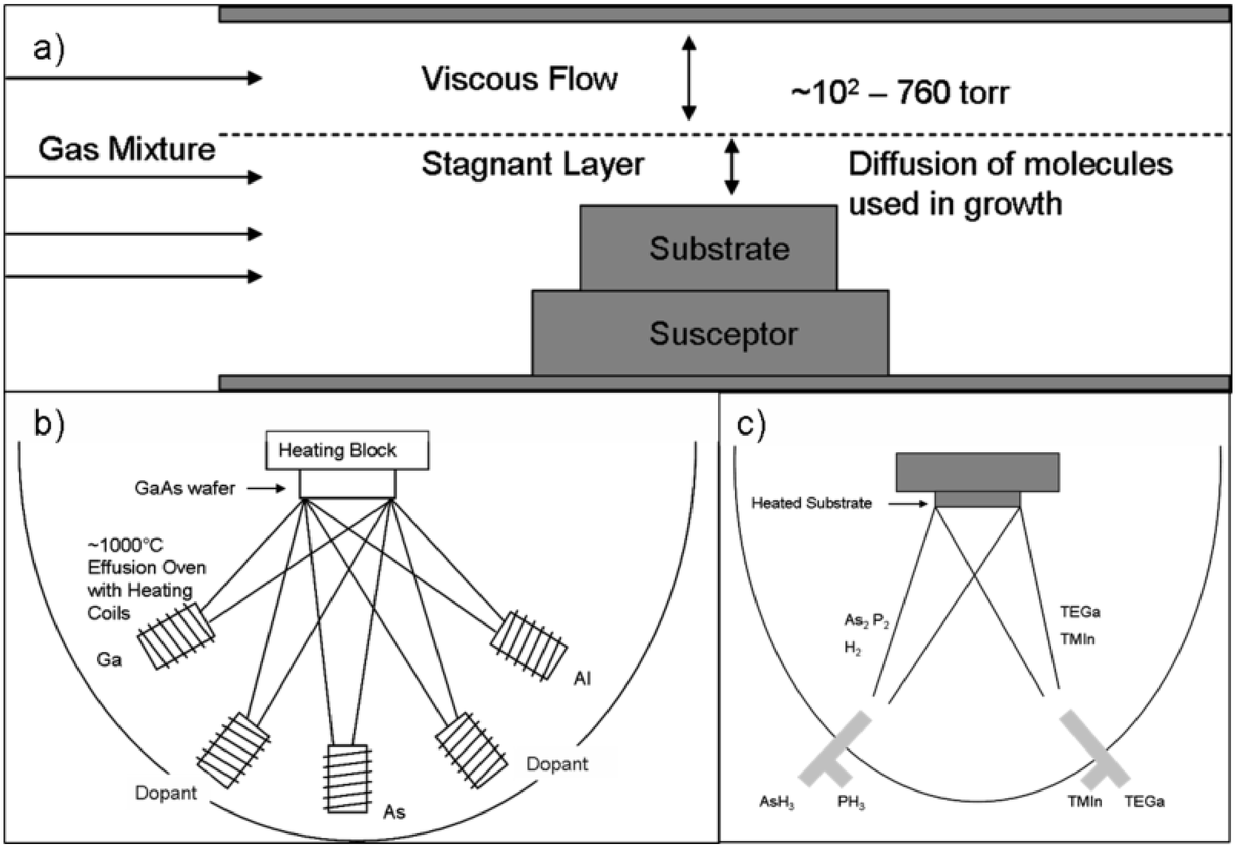

Figure 3.1: Schematics of the epitaxial growth processes involved in a) MOCVD, b) MBE and c) CBE

line/mm grating was used, giving a spectral coverage of approximately 700nm and a resolution of 1.4nm. A 600-line/mm grating was used for higher resolution spectroscopy, giving a spectral coverage of approximately 150nm and resolution of about 0.3nm. The continuous flow cryostat was able to cool the sample to a temperature of approximately 5K using pumped liquid helium from a 60L dewar. All photoluminescence spectroscopy was done at a temperature of 5K. The sample was fixed inside the cryostat and the entire cryostat was moved using a three-axis positioner to navigate around the sample and focus the laser spot.

To ensure the proper positioning of the excitation spot on a single quantum dot, an imaging system was used to observe the sample inside the cryostat. White light from a lamp was collimated and passed to the sample along the same path as the exciting laser. The white light was reflected from the sample surface and collected for imaging onto a CCD video camera. The sample surface could not be imaged while collecting spectra, instead a movable mirror was placed to reflect the white light back to the video camera and then removed when experimental data were collected. The experimental setup is schematically drawn in Figure 3.2 and shown in Figures 3.3 and 3.4.

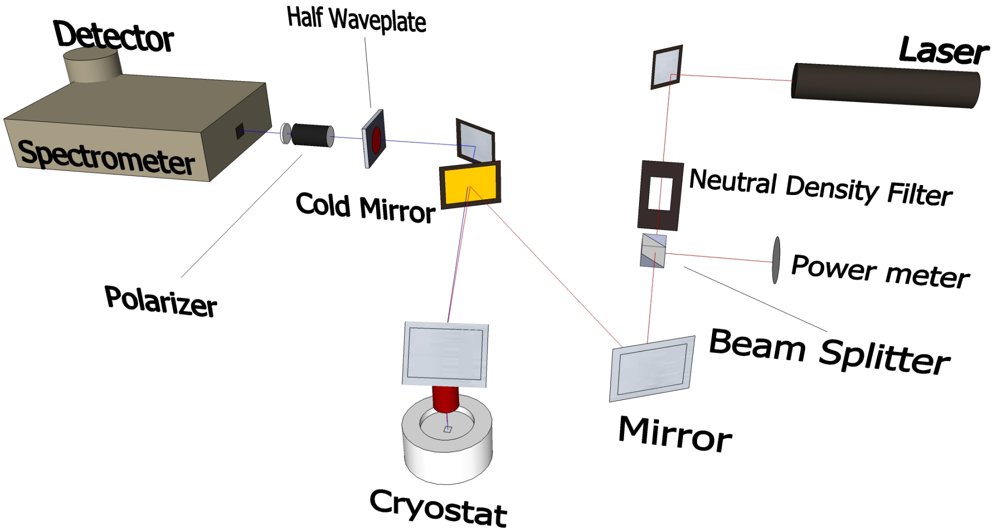

Figure 3.2: Schematic drawing of the photoluminescence spectroscopy setup used to optically characterize quantum dot samples.

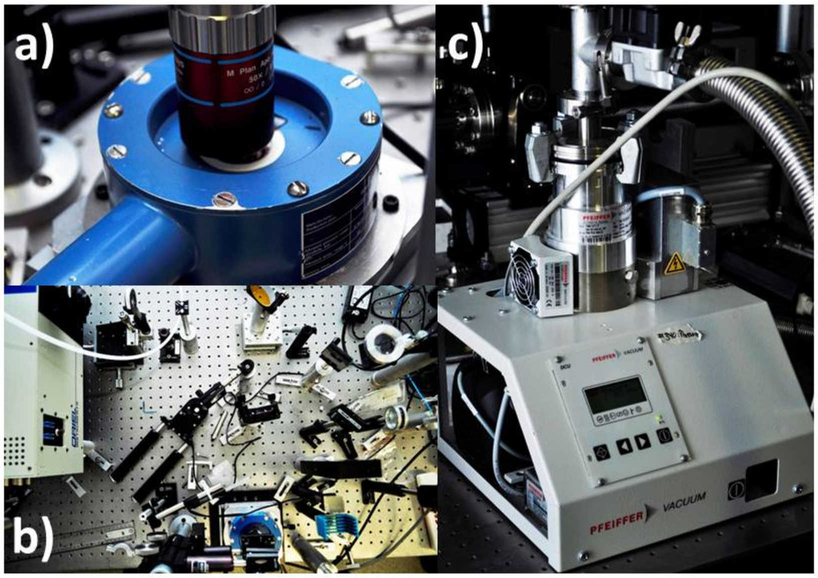

Figure 3.3: (a) The infrared objective lens system used to focus light onto a quantum dot, (b) a top-view of the optical table which holds the photoluminescence spectroscopy setup, and (c) a table top vacuum pump used to bring the cold finger cryostat to around 10^{-4} Pa.

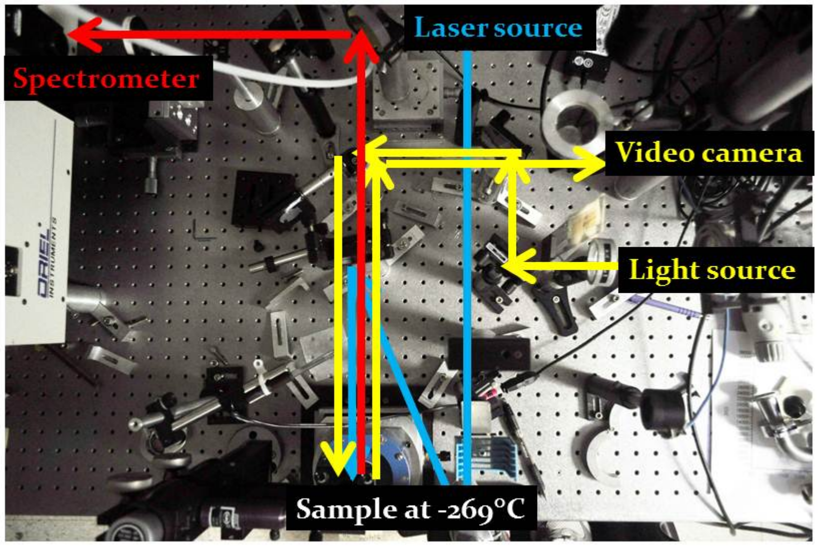

Figure 3.4: Top-view of the optical spectroscopy setup used to study quantum dots. The blue arrow represents the pump laser source at 632nm. The yellow arrow shows the path of the white light from the lamp in order to view the sample. The red arrow is the near-infrared photoluminescence from the dot that is collected into the spectrometer.

Chapter 4

Quantum dot nanotemplates

4.1 Introduction

Almost all of the isolated self-assembled quantum dots grown for research are designed to fulfill a proof-of-principle goal. In such cases, the spectroscopic study of a single dot is based either on precise positioning of the laser beam or on the statistical chance of a single dot existing within the laser spot. For the fabrication of devices in a scalable manner, these strategies are not practical.

To address the problem of scalability, a technique was developed using semiconductor nanotemplates that allows one to control the migration of surface adatoms deposited on the semiconductor surface during growth. Details of this growth process can be found in the literature[52, 53]. The semiconductor nanotemplate can be viewed as a non-planar InP nanostructure that controls the migration of materials deposited on its surface and directs the nucleation of individual quantum dots to occur at a selected spatial location. For our purposes, the ideal sample would consist of a small growth area (on the order of the size of a single quantum dot) and a large area upon which there would be no growth at all. This scenario would provide spatially isolated quantum dots. Ideally, the nanotemplate would exert strong constraints upon the quantum dot growth to ensure the best control over the quantum dot properties. The nanotemplates used throughout this thesis use crystallographic and geometric constraints on the quantum dot barrier material as an elegant, yet powerful way to best address the primary issues of quantum dot fabrication.

4.2 Growth of self-assembled InAs quantum dots on InP nanotemplates

The site-selectivity of single quantum dots fabricated under epitaxial conditions for the Stranski-Krastanov growth mode requires a properly treated semiconductor substrate. Exposing the entire substrate during the CBE growth process leaves a substrate covered in randomly positioned quantum dots. The resulting photoluminescence spectra reveals a broad Gaussian distribution curve indicative of a large ensemble of quantum dots.

The substrates used for the work in thesis are SiO_2-coated (001)InP wafers. Using electron beam lithography, the substrate is patterned with an array of submicron-sized squares. A precise wet etch process etches the SiO_2 to create square-shaped openings in the oxide exposing the InP as seen in Figure 4.1. Any growth on this oxide layer is forbidden as adatoms simply desorb from the oxide. The resulting nanostructure grows exclusively upon the exposed InP substrate. The SiO_2 layer is only 20nm thin to prevent shadowing of the growth material during the chemical beam epitaxy.

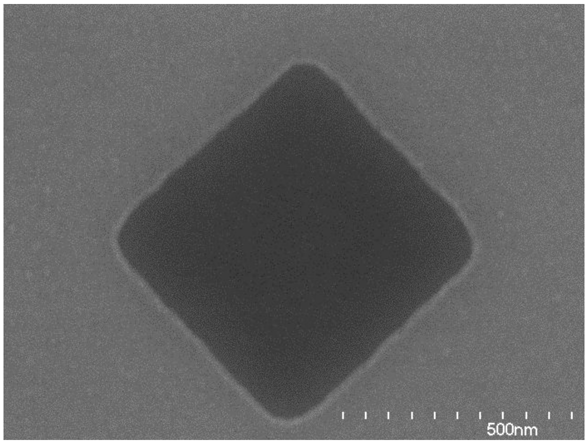

Figure 4.1: A single etched square through the SiO_2(lighter), exposing the InP substrate(darker) below.

The objective is to grow an InP nanotemplate upon the exposed substrate. This forms a perfectly smooth (001) InP surface upon which defect-free single dots can grow. The amount of InP grown on each etched square is constant during a single growth process. The side lengths of the etched squares are varied from 430nm to 500nm in 1.25nm increments. Ten repetitions of every square size are made. This creates a total of 500 nanotemplates per growth.

The fabrication of defect-free, high-quality quantum dots requires that the substrate to be atomically smooth. The exposed InP after the etching process does not result in a sufficiently smooth surface upon which to grow a quantum dot. The growth of quantum dots on this surface would create low-quality quantum dots.

In order to grow the InP nanotemplate and InAs quantum dots using CBE techniques, we require chemical sources of indium, arsenic and phosphorus. The CBE chamber at the Institute for Microstructural Sciences(IMS) is used for nanotemplate and quantum dot growth. The group III chemical inputs of the system are triethylgallium(TEG) and trimethylindium(TMI). The group V chemical inputs are arsine(AsH_3) and phosphine(PH_3). Firstly, the growth chamber is degassed at a temperature of 150°C to ensure a clean environment. Since we do not require gallium, TMI(an indium source) is injected into the growth chamber at the relatively low temperature of 100°C. The indium is the limiting factor in the growth of the nanotemplate and requires the gas ejection cell to face the substrate. The phosphine inputs are injected at a temperature of 950°C. The InP begins incorporating on the etched nanotemplate.

The growth of the nanotemplate is dictated by the crystallographic facets of InP. The indium and phosphorus atoms favour growth on the (001) plane over the {011} planes due to the lower surface energy of the (001) plane. The resulting nanotemplate begins to form a truncated square-based pyramidal structure as in Figure 4.4.

The growth of the InP pyramid continues until the top plateau of the pyramid approaches an area small enough to support only a single dot. The injection of phosphine is halted and arsine (AsH3) is introduced into the CBE chamber for two seconds. The arsenic forms an initial wetting layer followed by the strain-induced formation of a single quantum dot. An arsenic overpressure is maintained for ten seconds followed by a phosphorus overpressure for five seconds. TMI and phosphine are finally added to "cap" the dot, embedding the dot inside a completed InP pyramid. This capping is necessary to ensure proper three-dimensional confinement for the InAs dot. The sample is finally cooled to room temperature. Table 4.1 outlines the growth recipe of a dot embedded in a typical nanotemplate. The growth recipe was optimized by Dr. Dan Dalacu.

The surface area of the (001) facet is a geometric function of the growth time and pyramid side length, and therefore very tunable. A reduction in the growth time results in a larger top (001) plateau. This allows for either larger or multiple dots to form, as shown in Figure 4.2. From the control of the area of the top (001) plane, the number and size of dots can be tuned. Changing the size of the quantum dot changes the dot confinement properties and consequently their optical properties, as shown in Figure 4.3. Incremental differences in the sizes of the etched squares allow different stages of the nanotemplate growth process to be witnessed in a single CBE growth process.

Open Shutters	Duration	Chamber Temperature (°C)	Comments
None	10 seconds	25	Substrate held at 420°C
Phosphine	6 minutes	25→500	Ramp Temperature to 500°C
Phosphine	30 seconds	500	Hold at 500˙C
Phosphine	2 minutes	500→515	Ramp to 515°C
Phosphine	5 minutes	515	Oxide Removal
Phosphine	1.5 minutes	515	Ramp TMI
Phosphine	30 seconds	515	Stabilize prior to growth
TMI and Phosphine	37 minutes	515	Start InP pyramid growth
TMI and Phosphine	1 minute	515	Continue InP, prepare Arsenic
TMI and Arsine	2 seconds	515	Grow dots
Arsine	10 seconds	515	Apply arsenic overpressure
Phosphine	5 seconds	515	Apply phosphine overpressure
TMI and Phosphine	5 minutes	515	Cap pyramid
Phosphine	7 minutes	500→25	Cool down to 25°C

Table 4.1: Step-by-step InP nanotemplate and InAs quantum dot growth procedure in the CBE chamber. This recipe was used to grow the InAs/InP dots measured in this thesis.

This nanotemplate technique also lends itself to achieve control over the shape of the quantum dot. By etching a rectangular template into the oxide layer, the resulting structure is a rectangular pyramid where the surface of the (001) apex of the pyramid has a rectangular shape, also shown in Figure 4.2. The ability to control the shape of the quantum dot would allow one to engineer the excitonic g-factor of the dot. This g-factor engineering allows control over the magneto-optical properties of the dot. In the extreme limit of rectangular etches, long ridge-like structures can be grown with single or double rows of quantum dots on top[54]. For the purposes of this thesis, the etch pattern and growth conditions are tuned such that single, square dots are formed.

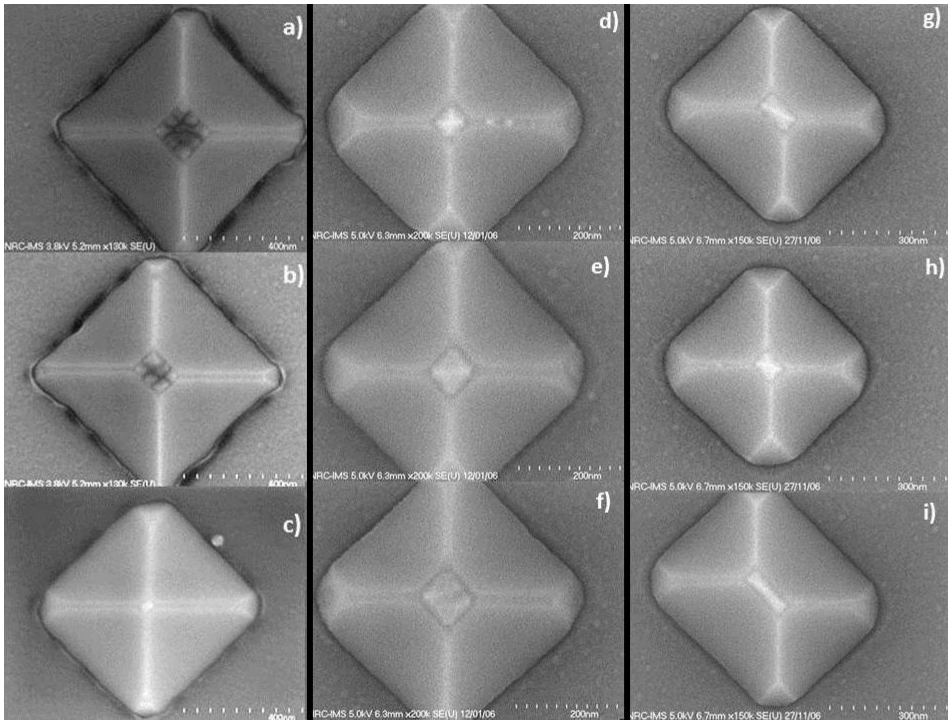

Figure 4.2: SEM micrographs of uncapped pyramids. In images (a), (b) and (c), the size of the etch patterns was changed to control the number of quantum dots created. In images (d), (e) and (f), the size of the quantum dot was tuned. In images, (g), (h) and (i) the etch patterns through the dielectric were varied, tuning the shape of the quantum dot from square to highly rectangular [48].

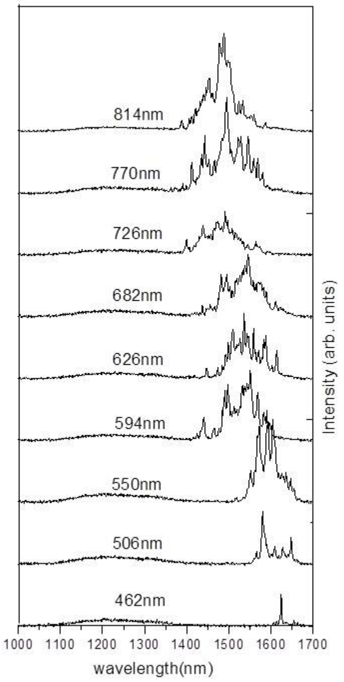

Figure 4.3: Photoluminescence spectra of single pyramids with decreasing side length (from 814 nm to 462 nm). As the area of the top (100) InP surface is correspondingly reduced, the number of photoluminescence peaks from individual dots drops, indicating a reduction in the number of quantum dots. As the pyramid side length is decreased, the number of dots is decreased and the average emission energy of the dots is red-shifted [48].

In summary, the site-selectivity of single quantum dots is achieved using patterned etches through a thin SiO_2 coating upon which the growth adatoms cannot incorporate. The size of the apex of the truncated pyramid is controlled by careful tuning of the nanotemplate growth time. Adatoms from the epitaxial process accumulate upon the (001) plane over the {011} crystallographic planes resulting in the a truncated pyramidal growth process. The fabrication of an embedded single dot within the pyramidal nanotemplate is schematically outlined in Figure 4.4.

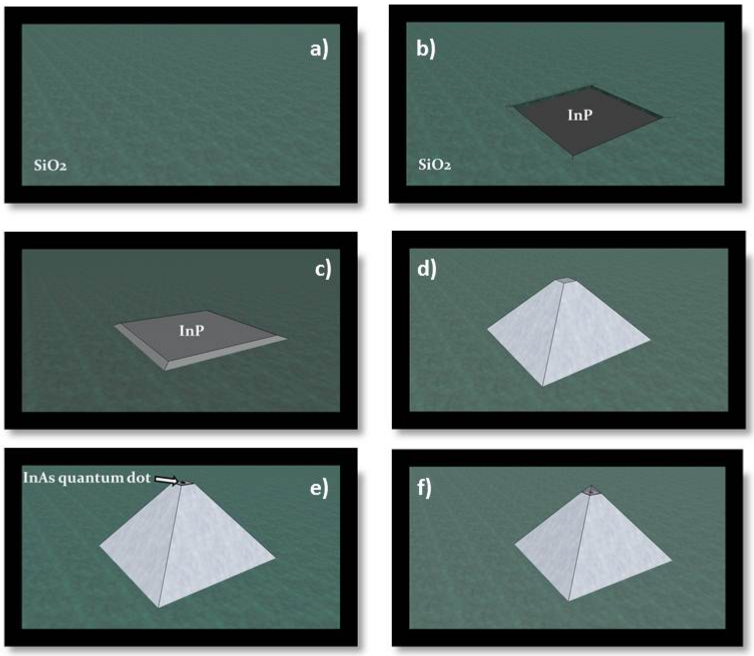

Figure 4.4: (a)The SiO_2 mask is sputtered on the (001) InP substrate, (b) A square is etched through to the InP below (c) The growth of the InP nanotemplate begins (d) the growth is stopped prior to the completion of the pyramid (e) InAs is grown on top forming a single quantum dot (f) The pyramid is capped with additional InP to enclose the InAs to form the quantum dot.

4.3 Photoluminescence of single InAs quantum dots on InP nanopyramids

InAs/InP quantum dots are typically not of the same quality as InAs/GaAs quantum dots due to the differences in the interfacial strain and the maturity of the fabrication processes. However, recent progress in growth procedures of InAs/InP quantum dot systems have produced very bright single dots embedded in pyramidal nanotemplates[48]. The observation of single dots is now routine and the photoluminescence spectrum is well characterized. Much like InAs/GaAs dots[55], the fine-structure of InAs/InP quantum dots reveals a multitude of states in the photoluminescence spectra. The typical single dot in a pyramid emits photons with wavelengths around 1.5μm with the X^{-1} state being dominant due to electrons in the wetting layer tunneling into the dot during an electron-hole recombination event. The X^0 transition is present at a slightly higher energy. The XX transition appears at higher optical excitation powers while the exciton peak intensity saturates. The photoluminescence at low pump intensities of a typical single dot as a function of energy is shown in Figure 4.5.

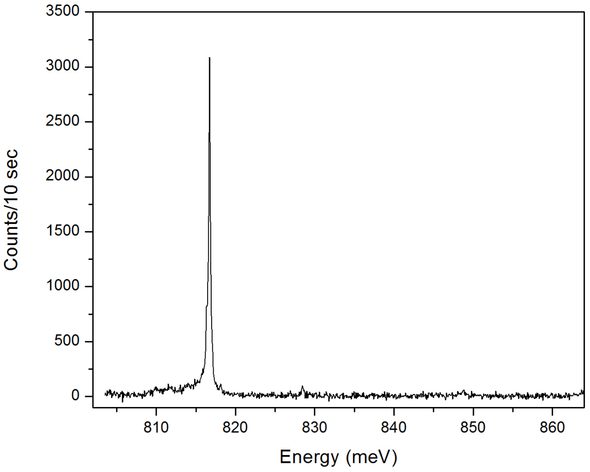

Figure 4.5: Photoluminescence of a single dot in a pyramid at a temperature of 4K with low optical pump power. The linewidth of the peak is resolution limited. In this dot, the emission wavelength is about 1.52μm, which is nearly ideal for fibre-based transmission.

The biexciton transition appears beside the exciton transition at higher powers. The p states are not degenerate as they are highly sensitive to the asymmetric confining potential of the dot. Highly excited transitions can be seen with higher pump powers in Figure 4.6.

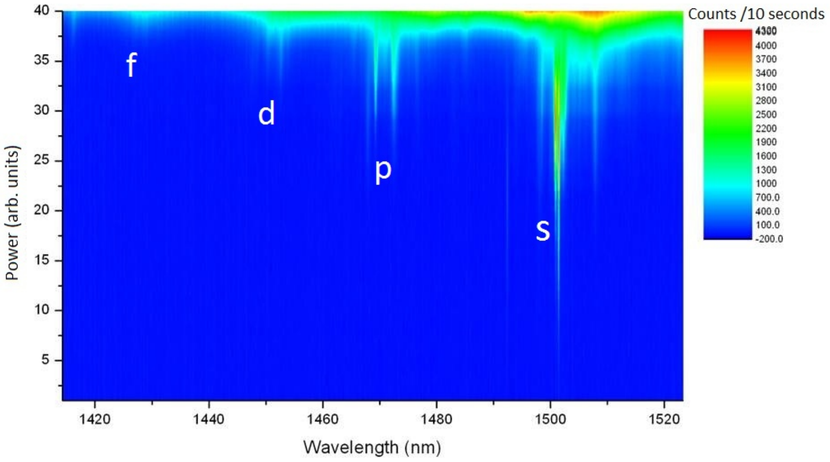

Figure 4.6: Power spectrum of a single dot in a pyramid. The s, p, d and f states are clearly visible with increasing laser power.

The resolution of the linewidth of the X^0 state is restricted by the technical limitations of the spectrometer and CCD detector as shown in reference as shown in Figure 4.7. The linewidth is smaller than the measured full width at half maximum.

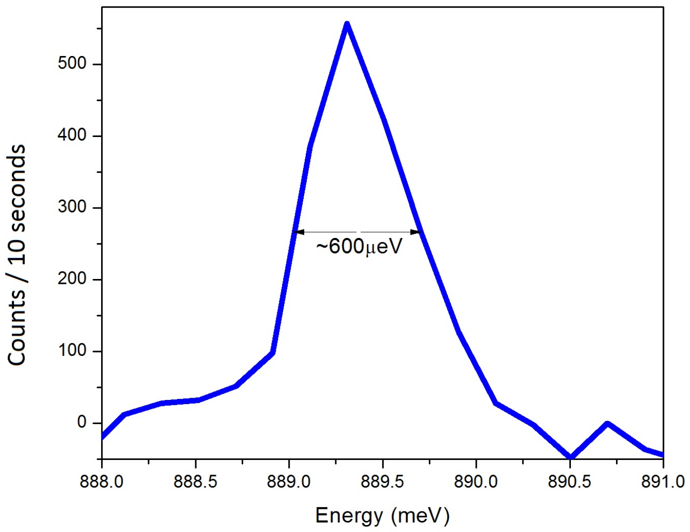

Figure 4.7: Single photoluminescence peak from a quantum dot. The full width at half maximum of the excitonic transition is resolution-limited, indicative of good confinement in the quantum dot.

4.4 Chapter summary and comments

In summary, InP pyramidal nanotemplates are grown using a site-selective CBE growth process. Single InAs dots are deposited upon the (001) surface of the truncated pyramid before being capped with additional InP, completing the nanotemplate. Physical properties of the dots such as the size, number and shape can be tuned by the geometric constraints of the nanotemplate growth. Photoluminescence spectroscopy of the dots reveals resolution-limited peaks resulting from emitted photons around the optimal wavelength of 1.55μm. Stronger optical excitation of a single dot permits the identification of grouped p, d and f exciton states.

Chapter 5

Electrostatic gating of InAs quantum dots

5.1 Introduction

The confining potential of each self-assembled dot is dependent on its size, composition and shape; properties that cannot be easily changed following the initial growth process. Using electric fields, the confining potential of a dot can be tuned after the initial growth process. Vertical fields can be used to control the position of the Fermi level relative to the bottom of the confining potential, changing the number of confined electrons and holes. Lateral electric fields can control the overlap of the confined electron and hole wavefunctions. By using a localized gating strategy, the charge state and energy of the exciton states of a dot can be engineered for complete control over the photons emitted from a single dot.

For any quantum dot, there are four distinct neutral exciton (X^0) states corresponding to the four possible spin configurations of the electrons and holes. Using bra-ket notation ($|J, m_j\rangle$), where J is the total angular momentum of the electron and hole, and m_j is the magnetic quantum number, we may label them as $|2, -1\rangle$, $|2, 1\rangle$, $|2, 2\rangle$ and $|2, -2\rangle$. Excitons with parallel electron and hole spins, $|2, 2\rangle$ and $|2, -2\rangle$, are called "dark excitons". These excitons have long radiative lifetimes and do not readily recombine to emit a single photon because of the the need to conserve angular momentum. Excitons with opposite electron and hole spins, $|2, -1\rangle$ and $|2, 1\rangle$, are called "bright excitons" and can emit photons after the electron and hole recombine.

For an ideal dot with a radially symmetric confining potential, photons emitted from the two bright exciton recombination processes are indistinguishable in energy and opposite in polarization. However, due to the crystallographic orientation of the substrate and epitaxial growth conditions, virtually all of dots are irregularly-shaped. This results in an asymmetrically-shaped confining potential for the dots, which removes the degeneracy of the two different spin configurations of the bright exciton. The emitted photons from the two bright exciton transitions can be isolated and identified using a half-wave plate and a linear polarizer. The splitting between the exciton states is often referred to as the fine-structure splitting (FSS), exchange splitting, or anisotropic exchange splitting (AES), and is on the order of a few hundred μeVs for the InAs/InP dots studied here. The cascades of transitions from the biexciton state to the vacuum state for dots with symmetric and asymmetric confining potentials are shown in Figure 5.1.

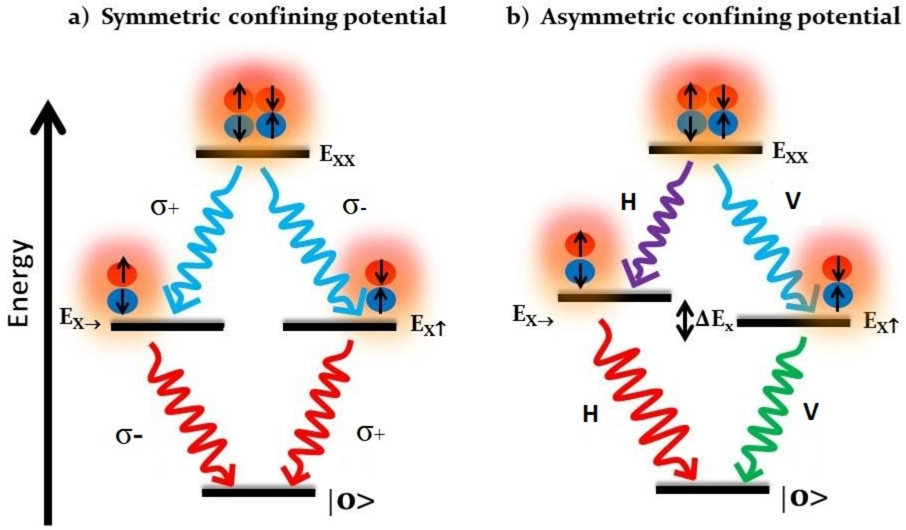

Figure 5.1: The biexciton cascade for a dot with (a) a symmetric confining potential and (b) an asymmetric confining potential. $\sigma+$ and $\sigma-$ represent the right and left circularly polarized photons. The photons states on the right are linear combinations of right and left circularly polarized states due to the breaking of the symmetry of the dot. E_{XX} represents the biexciton state, $|0\rangle$ is the vacuum state, and $E_X \rightarrow$ and $E_X \uparrow$ represent the neutral exciton(X) states emitting $\rightarrow$ and $\uparrow$ polarized photons, respectively. The splitting between the two bright exciton states is labeled as ΔE_X. The black arrows indicate the spin of each particle.

The biexciton cascade in quantum dots is a promising candidate as a source of on-demand entangled photons[15, 56]. The "which-path" information of emitted photons from dots with degenerate exciton states is removed and the photons are polarization-entangled. One of the major hindrances to this goal is the lack of control over the geometry of the confinement potential of a single dot. In principle, electric fields perpendicular to the growth axis of the dot can be used to control the symmetry of the confining potential, controlling the entanglement of emitted photons.

Alternatively, the need for degenerate exciton states can be circumvented through lateral field tuning of the biexciton binding energy[57, 58]. If the exciton and biexciton transitions are degenerate, the emitted photons from both transitions can be entangled. However, the success of this scheme is limited to dots where the biexciton and exciton states are nearly degenerate, due to the small practical tuning range of the biexciton binding energy. Tuning the geometry of the confinement potential of a single dot may be a more elegant solution. In this chapter, we discuss the gating of the pyramidal nanotemplate and the effects of vertical, lateral and quadrapole electric field configurations on the charge state and fine structure of the dot.

5.2 Fabrication of electrostatic gates

Most studies of gated dots have concentrated on the Stark effect and the various charge states[59]. These experiments generally rely on the application of electric fields using a macroscopic field-effect structure biased with respect to a back gate to demonstrate control over the charge state of an ensemble of dots[60, 61]. These methods do not allow for precise control over the dot confinement geometry and cannot be practically implemented in a scalable quantum information architecture. At the Institute for Microstructural Sciences of the National Research Council of Canada, a localized gating configuration was devised which ensures compatibility with the pyramidal nanotemplate.

To experimentally realize a localized electric field, gates were deposited very close to the quantum dot. To accomplish this, Au/Ti gates were deposited using an e-beam-defined polymethyl methacrylate (PMMA) lift-off process aligned using dry-etched trenches in the substrate, 50 μm from the pyramid. The gates were positioned along the {011} sidewalls of the pyramid. The alignment of the gates to the centre of the pyramidal nanotemplate has an accuracy better than 50 nm. The lithography is set such that there is one pyramid per e-beam write field with each field consisting of a set of alignment trenches. A design of one gate per pyramidal sidewall was chosen as it allows for control over the direction of the electric field and is relatively straightforward to fabricate. This also presents an opportunity to control the quantum dot confining

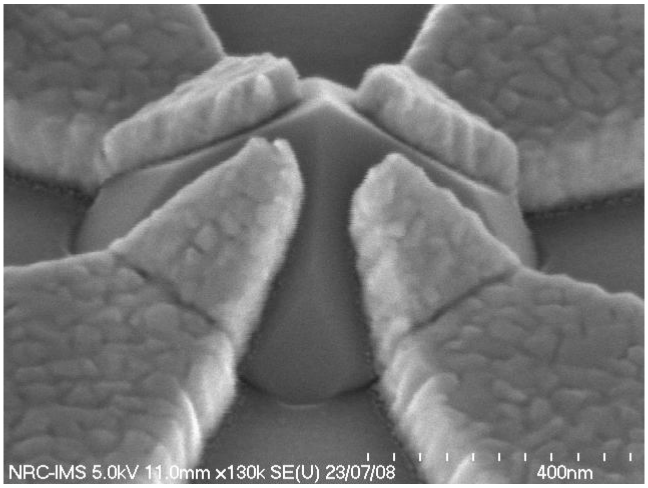

Figure 5.2: The pyramidal nanotemplate with metallic gates on the sides. The quantum dot is embedded inside near the top of the pyramid [47].

potential using vertical, lateral or quadrapole electric field configurations. An SEM micrograph of the gated nanotemplate is shown in Figure 5.2.

A vertical field is created by applying a voltage between the top four gates (on the pyramid) and a back gate (below the substrate). A lateral field can be generated by applying a voltage between opposite top gates. Additionally, a quadrapole-type field can be created using two positively-biased and two negatively-biased gates, where the similarly-biased gates are positioned opposite each other. The quadrapole field gating configuration produces a distinct saddle-shaped potential with the dot located at the origin. A schematic of a quadrapole field configuration is shown in Figure 5.3.

The effective electric field experienced by the dot is dependent on the current-voltage characteristics (or I-V curves) of the gates. An ideal Schottky gate would demonstrate zero leakage current in reverse bias and very low resistance in the forward bias regime. Reverse bias is defined as biasing the top gates negatively with respect to the back gate. A leaking gate would reveal a more linear I-V curve, which is characteristic of an ohmic contact. Slight differences in the metal-semiconductor interfaces between the gates and the pyramid result in different I-V curves for each gate. The variability in quality of these interfaces reflects the challenge of creating four identical gates. The I-V curves for each of the four gates on the sides of a pyramid are shown in Figure 5.4.

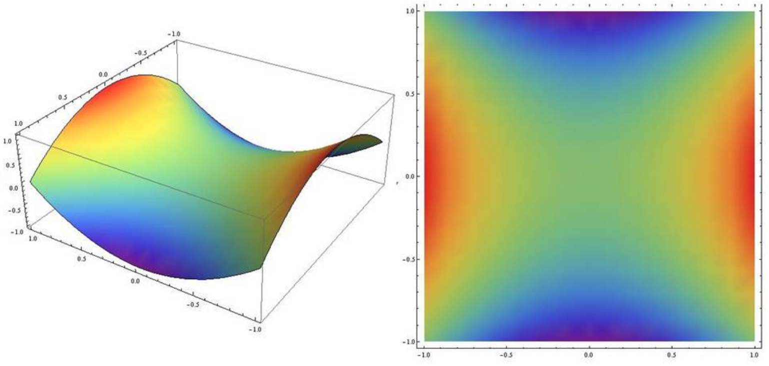

Figure 5.3: Quadrapole electric field as (a) a 3D surface plot and (b) a 2D colour map. The colour and height of the surface represents the electric field.

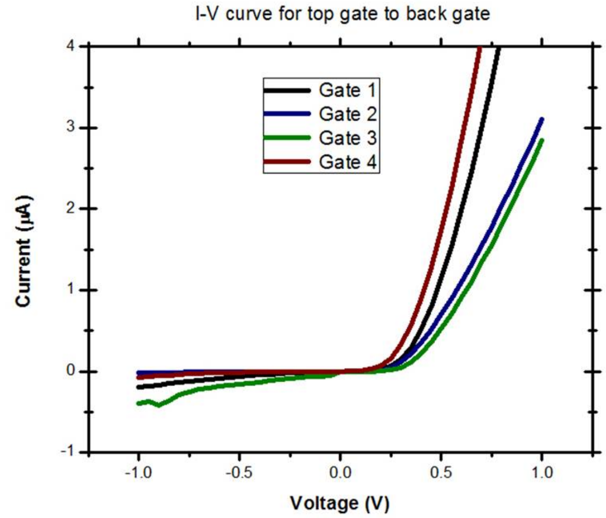

Figure 5.4: IV curves of four functioning gates on the sidewalls of a pyramidal nanotemplate. The low leakage current to the substrate at negative top gate voltages permits the application of an electric field across the dot. The differences between the IV curves reflect inevitable differences in the quality of each gate.

5.3 Bond pads and wire bonding

Gates are deposited along the sidewalls of the pyramidal nanotemplate prior to the optical characterization of the dots in order to make it easier to locate each pyramid. Pyramids with a photoluminescence spectrum revealing a few bright, narrow-linewidth peaks are selected to have four bond pads deposited around them. Typically, about 20% of all pyramids contain spectrally-isolated single dots. The bond pads are thin Au/Ti sheets which enable the connection of macroscopic voltage sources to the microscopic gates on the pyramid. The bond pads are square in shape and have side lengths of 100 μm.

Once the sample has four bond pads placed around each chosen pyramid, the chip is cleaved into about 5-9 smaller chips. Each small chip is small enough to fit inside a Kyocera® chip mount. The chip mounts are small stages containing eight electrical contacts wired to pins to facilitate connecting small electronic chips to larger voltage sources.

Prior to mounting the sample, the chip mounts are cleaned in acetone for five minutes, and immersed in isopropanol for another five minutes before being dried. Silver epoxy is used to affix each chip to the chip mount. The gold-plated surface of the chip mount acts as the back gate for each gated pyramid. The chip mounts are then placed into an oven for an hour at a temperature of 120°C to accelerate the adhesion of the chip to the silver epoxy. Thin gold wires are used to connect the bond pads to the pin contacts of the chip mount. A wire bonding machine heats the gold wire to about 45°C and uses ultrasonic pulses to fuse the gold wires to the bond pads. A photograph of a sample wired to a chip mount is shown in Figure 5.5.

The pins of the sample holder fit into an 8-pin socket inside the low-temperature, windowed cryostat. The socket is wired to a 4-port digital-to-analog power supply (DAC448/4) where computer software controls the voltage at each top gate. An electrometer is used to apply a voltage to the back gate with respect to the top gates to apply a vertical field. Figure 5.6 details the electrical configuration of a gated sample.

One consequence of gating the pyramid to a macroscopic voltage source is the increased risk of destroying the pyramid through static electricity. If the gates of the pyramid are not properly grounded, shorting of the gates through the pyramid can result in its partial or complete destruction. Precautions are taken to reduce the risk of destroying the gated sample whenever handling of the pyramid is necessary. Grounding the wrist, tweezers, and all electrical contacts while handling the sample largely prevents damage to the gated pyramid. An SEM micrograph of a gated pyramid sample

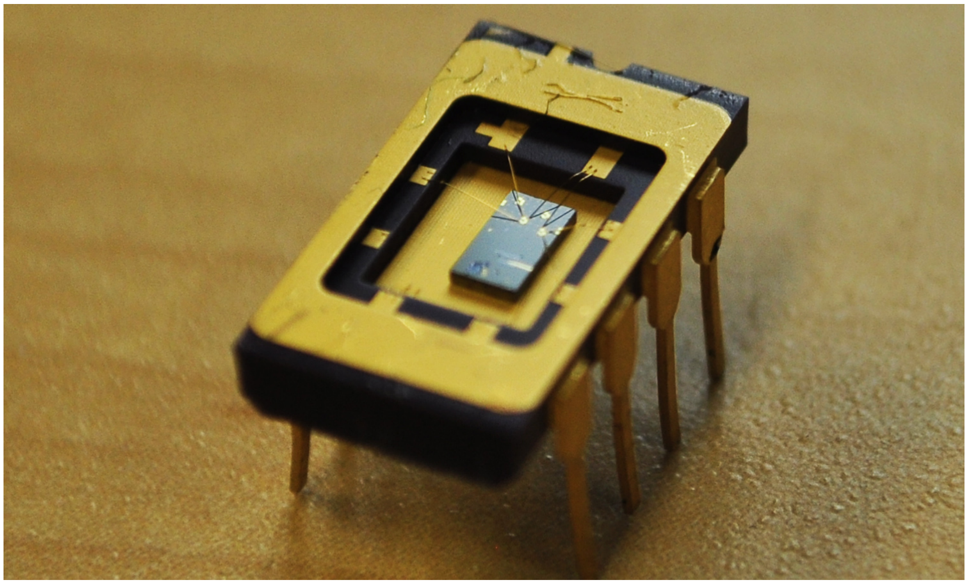

Figure 5.5: Picture of a sample in a chip mount. The chip mount has eight pins which connect through to the top of the mount. For this sample, two pyramids are gated. The four bond pads for each dot are connected to four separate pins. One pin may be used to connect to more than one dot. One pin is connected to the surface of the chip mount, creating an electric contact below the substrate.

destroyed through improper grounding is shown in Figure 5.7.

5.4 Exchange splitting

Various techniques to tune the exchange splitting of the exciton states in the biexciton cascade have been explored. Rapid thermal annealing (RTA) of quantum dots has been shown to tune the exchange splitting of the exciton for InGaAs/GaAs dots[62]. RTA of quantum dots is accomplished by rapidly heating the substrate which influences the in-plane symmetry of dots. The major drawbacks of this technique include the irreversibility of the process, and the inability to anneal individual dots independently. Other methods include using magnetic or electric fields to control the confining potential of the quantum dot[63, 64]. While magnetic fields can be used to tune the exchange splitting, the difficulty involved in creating a strong, localized magnetic field conflicts with the advantageous properties of a scalable system. Meanwhile, gated quantum dot systems can provide a route to a localized and scalable entangled photon source.

To distinguish between two nearly-degenerate states, the polarization of the photoluminescence from a single dot must be measured. To excite the dot, a laser beam is focused onto a single pyramid. The photoluminescence is collected and passed through

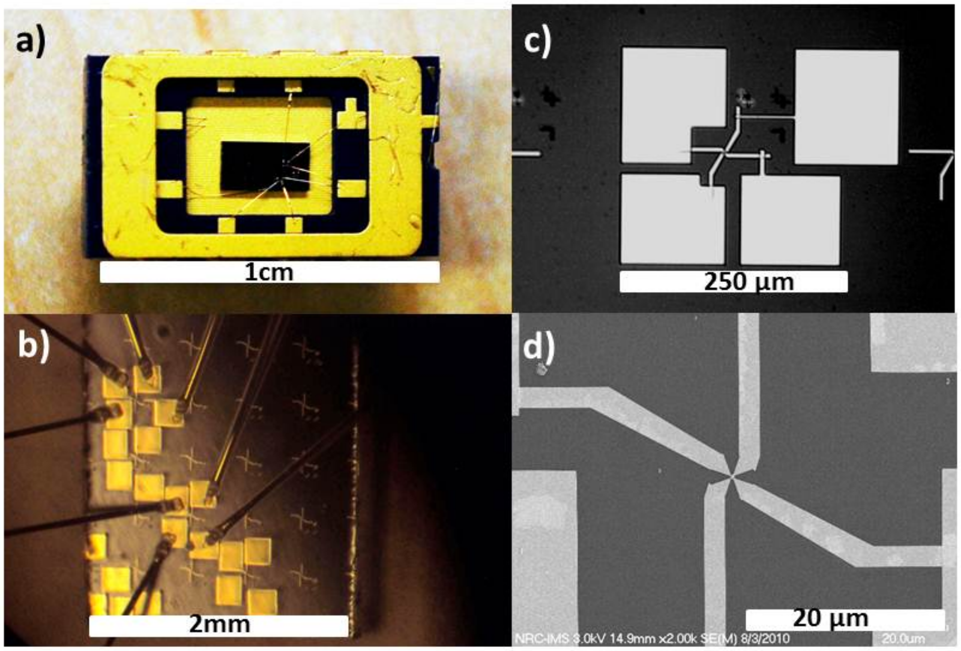

Figure 5.6: (a) A chip mount with two pyramids wire-bonded to the gating pins, (b) an optical micrograph of gold wires bonded to the four bond pads of each pyramid, (c) an optical micrograph of a pyramid with four deposited bond pads which has not been wire-bonded, (d) an SEM micrograph of four gates connecting the bond pads to the pyramid

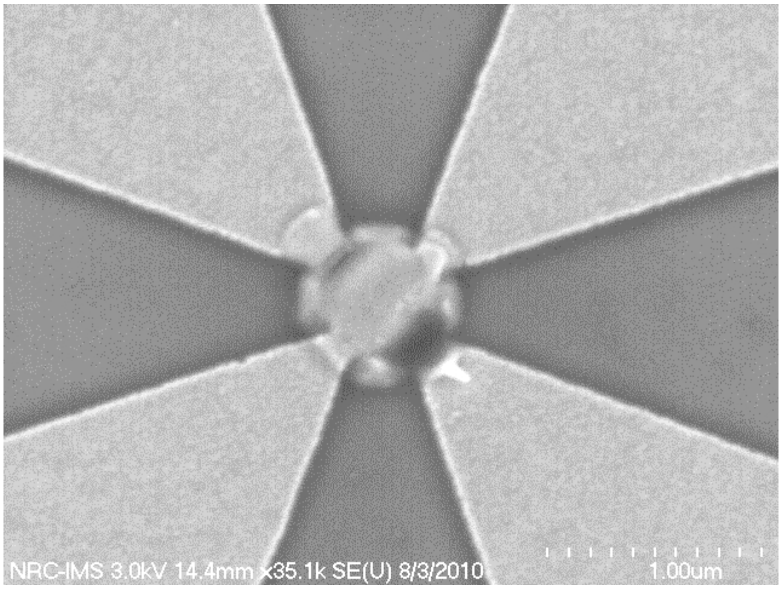

Figure 5.7: An SEM micrograph of a completely destroyed gated pyramid. If the gates are subject to a large spike in voltage due to static electricity, the gates are shorted and the pyramid is destroyed.

a half-wave plate and a Glan-Thompson polarizer prior to entering the spectrometer, which isolates a single path of the biexciton cascade. The half-wave plate rotates the polarization of the emitted photons by an angle of 2θ, where θ is the angle between the optical axis of the wave plate and the polarization of the emitted photons. The Glan-Thompson polarizer allows a single linear single polarization to pass through. The angle of the half-wave plate effectively controls which path of the biexciton cascade is visible. The photons which pass through the polarizer are focused onto the slit of the spectrometer and collected at the detector. The additional optics of the half-wave plate and Glan-Thompson polarizer reduce the detection count rate by approximately 20%. A schematic of the polarization optics used to identify each exciton recombination path is shown in Figure 5.8.

The exchange splitting of the X^0 state of a typical InAs/InP dot ranges from 150 μeV to 250 μeV at zero external field. The maximum spectral resolution of the spectrometer is about 150 μeV, which is insufficient to completely resolve the photons from each exciton recombination path. However, an exchange splitting can be verified by an oscillatory shifting of the emission peak as a function of wave plate angle, where the photoluminescence from one transition is blocked. The photoluminescence as a function of wave plate angle is measured and imported into a an algorithm which fits a Lorentzian peak to the emission peak. The centre of the peak is extracted from the Lorentzian function and is plotted as a function of wave plate angle. The exchange splitting

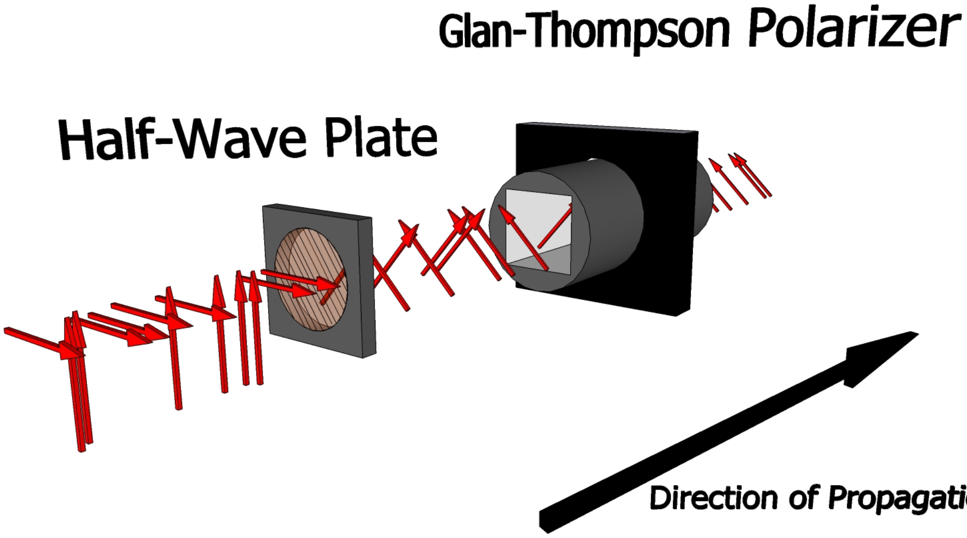

Figure 5.8: Schematic of the polarization optics used to isolate and identify the photoluminescence from each exciton transition. The half-wave plate rotates the polarization of the photons 2θ degrees. The parallel lines on the half-wave plate indicate the optical axis. The photons polarized in the same direction as the optical axis of the Glan-Thompson polarizer can pass through to the spectrometer.

is measured as the difference in energy between the minimum and maximum of the resulting sinusoidal function. Using this fitting algorithm, exchange splittings as low as ten μeVs can be resolved.

If a higher laser power is used, photoluminescence from the decay of the biexciton state increases quadratically. The exchange splitting of the biexciton state can be measured analogously to that of the exciton. Due to the biexciton cascade, the measured exchange splitting of the XX and the X^0 transitions are intimately related. The phase of the X^0 and XX emission peaks as function of wave plate angle are exactly opposite. The positions of the emission peaks for the X^0, XX and X^{-1} states as a function of half-wave plate angle are shown in Figure 5.9. The exchange splitting is extracted as twice the amplitude of a fitted sinusoidal function. The XX and X^0 states were conclusively identified by an out-of-phase oscillation of two emission peaks. The X^{-1} state is identified by an exchange splitting of zero. The emission peak corresponding to the X^{-1} state does not shift as a function of the wave plate angle. The two electrons in the X^{-1} state can be viewed as a singlet state. Since there is no exchange interaction between a singlet and a hole, the exchange splitting vanishes as illustrated in Figure 5.9.

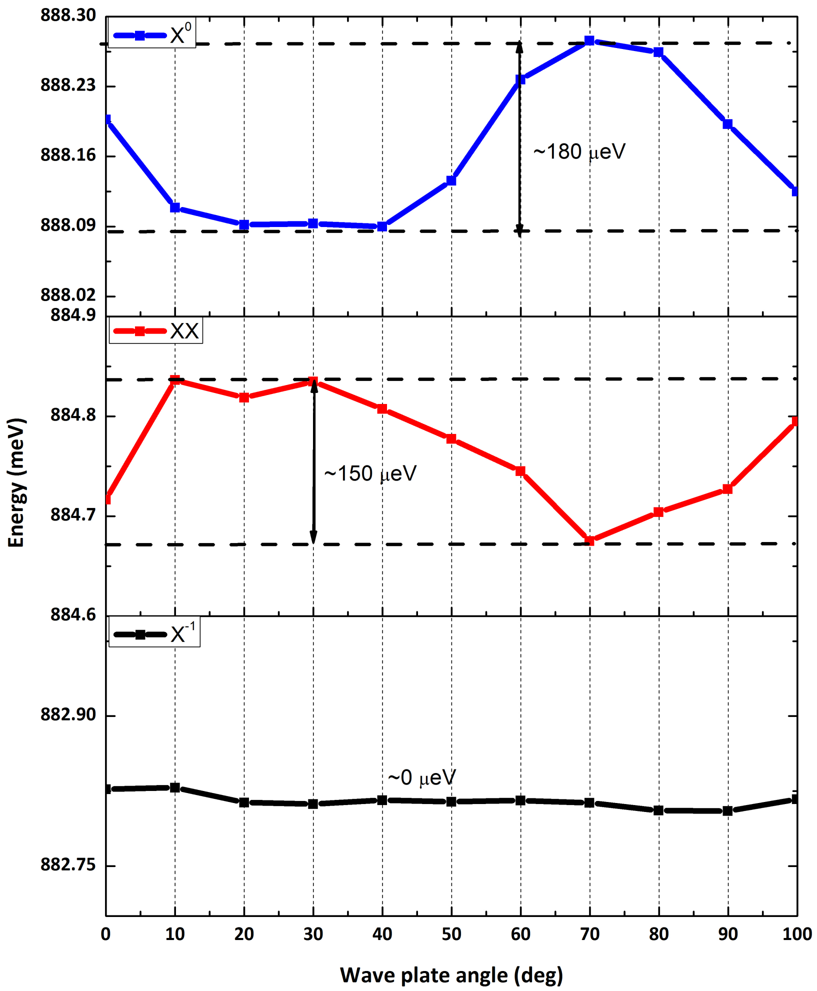

Figure 5.9: Plot of the energy of photoluminescence peaks for the X^0, XX and X^{-1} states as a function of half-wave plate angle. The exchange splitting is extracted from a fitted sinusoidal function. The phases of the X^0 and XX states are opposite. There is no exchange splitting for the X^{-1} state. Each data point has a peak position error of about $\pm 10 \mu eV$, while the error on the wave plate angle is negligible.

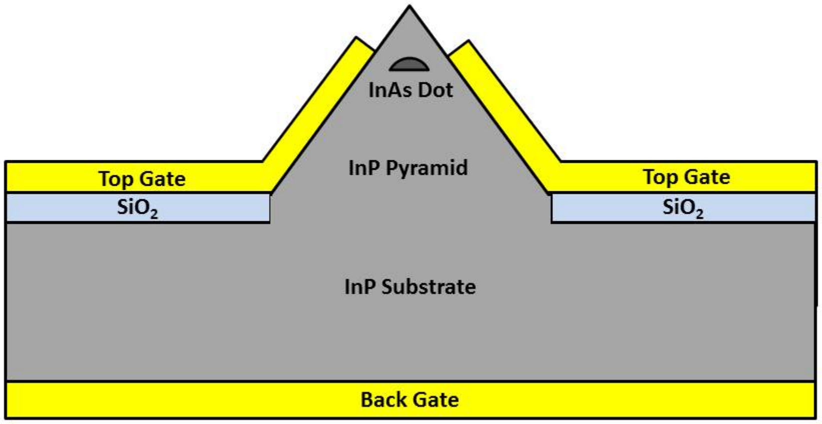

Figure 5.10: Cross-section schematic of the vertical gating configuration on a pyramidal nanotemplate. The top gates are biased with respect to the back gate, generating a vertical electric field across the quantum dot.

5.5 Vertical electric field

A vertical field has been utilized in previous work to control the charge state of a quantum dot[65]. A back gate enables the application of an electric field parallel to the growth axis of the dot when biased with respect to the four top gates. A schematic of the vertical gating scheme is shown in Figure 5.10. By increasing the vertical field, the dot can be emptied or filled with electrons, changing the charge state. A Coulomb-induced renormalization due to an extra electron in the dot shifts the energy of the photoluminescence peak by a few meVs. The photoluminescence of a single dot as a function of vertical electric field intensity is shown in Figure 5.11.

When there is no bias applied, excess electrons in the wetting layer can tunnel into the quantum dot and form charge states. The X^{-1} charge state is identified using polarization optics by its zero exchange splitting. With the addition of a vertical field, excess electrons from the wetting layer can be blocked from tunneling into the dot, resulting in photons emitted from the charge-neutral exciton (X^0) state. With the addition of a stronger vertical field, the quantum dot is completely depleted of electrons

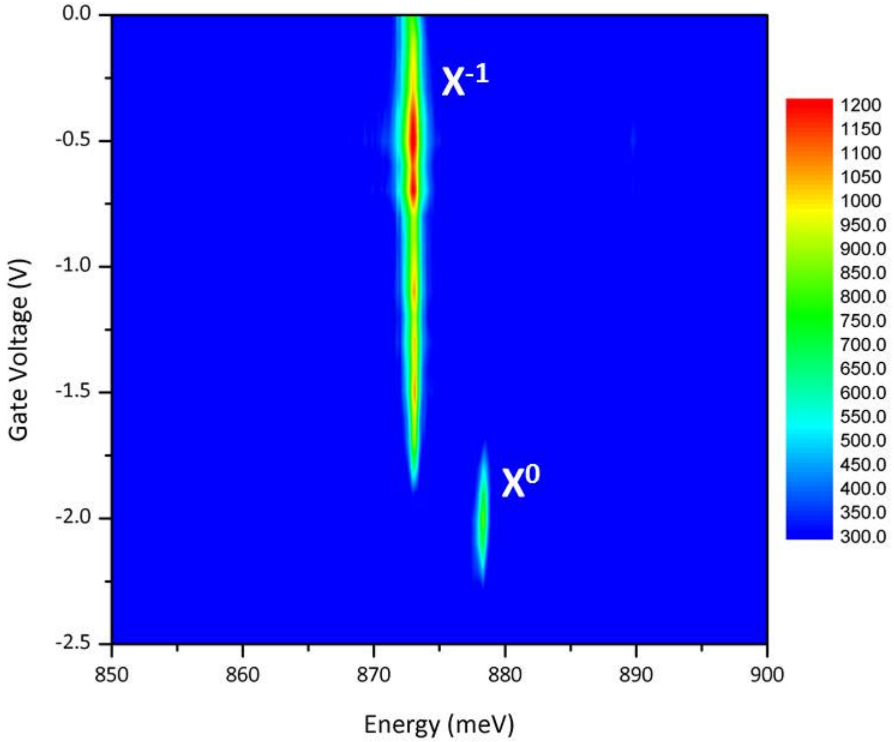

Figure 5.11: Photoluminescence from a single dot as a function of voltage between the top gates and the back gate. The laser power was set at 2 μW. As the voltage increases, the vertical field increases, and electrons are progressively emptied the dot from two electrons (X^{-1}), to one electron(X^0) to none.

and no electron-hole recombination processes can occur. The charge state is identified as X^{-1} (as opposed to X^{+1}) as it appears at a lower energy than the X^0 state because the binding energy of two electrons is larger than that of two holes in this dot system.

5.6 Lateral electric field

In principle, the top gates on the pyramid can produce a lateral electric field by applying a voltage between two opposite gates, as shown in Figure 5.12. This type of field can tune the lateral overlap of the confined electron and hole wavefunctions, affecting the electron-hole recombination rate and the exchange splitting.

To illustrate the effect of a lateral field on a single quantum dot, the confined electron and hole wavefunctions can be modeled as one-dimensional harmonic oscillator states in the presence of a linear electric field. The one-dimensional confining potential for a

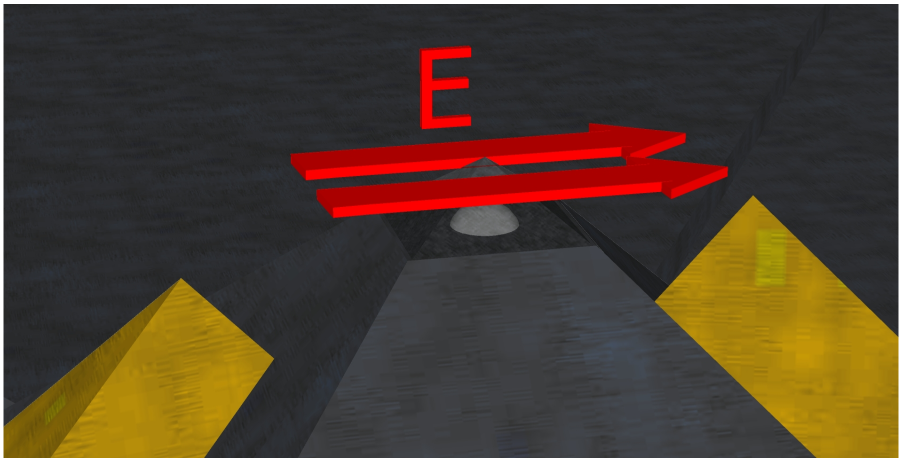

Figure 5.12: Schematic of the lateral gating configuration. A voltage is applied between the left and right top gates to create a lateral electric field component across the dot.

particle in a dot is thus parabolic, having the form

$$V(x) = \frac{1}{2} m_e^* \omega_e^2 x^2 - eEx, \tag{5.1}$$

where m_e^* is the effective mass of the electron, ω_e is the oscillator frequency, E is the electric field and e is the elementary charge.

By completing the square, we can rearrange the above equation in terms of a shift in the parabolic potential,

$$V(x) = \frac{1}{2} m_e^* \omega_e^2 \left(x - \Delta x_e\right)^2 - \frac{eE}{2} \Delta x_e \tag{5.2}$$

where the shift in the electron confining potential is

$$\Delta x_e = \frac{eE}{m_e^* \omega_e^2}. \tag{5.3}$$

The last term $\frac{eE}{2}\Delta x_e$ shifts the depth of the confining potential resulting in the Stark shift. Analogously, the shift of the hole confining potential is

$$\Delta x_h = \frac{-eE}{m_h^* \omega_h^2}, \tag{5.4}$$

with the hole parameters denoted with subscript "h".

The electron and hole confining potentials are shifted farther from each other, resulting in a reduction in the overlap of electron and hole wavefunctions. As a consequence, the oscillator strength is reduced and the exchange splitting of the exciton decreases[57].

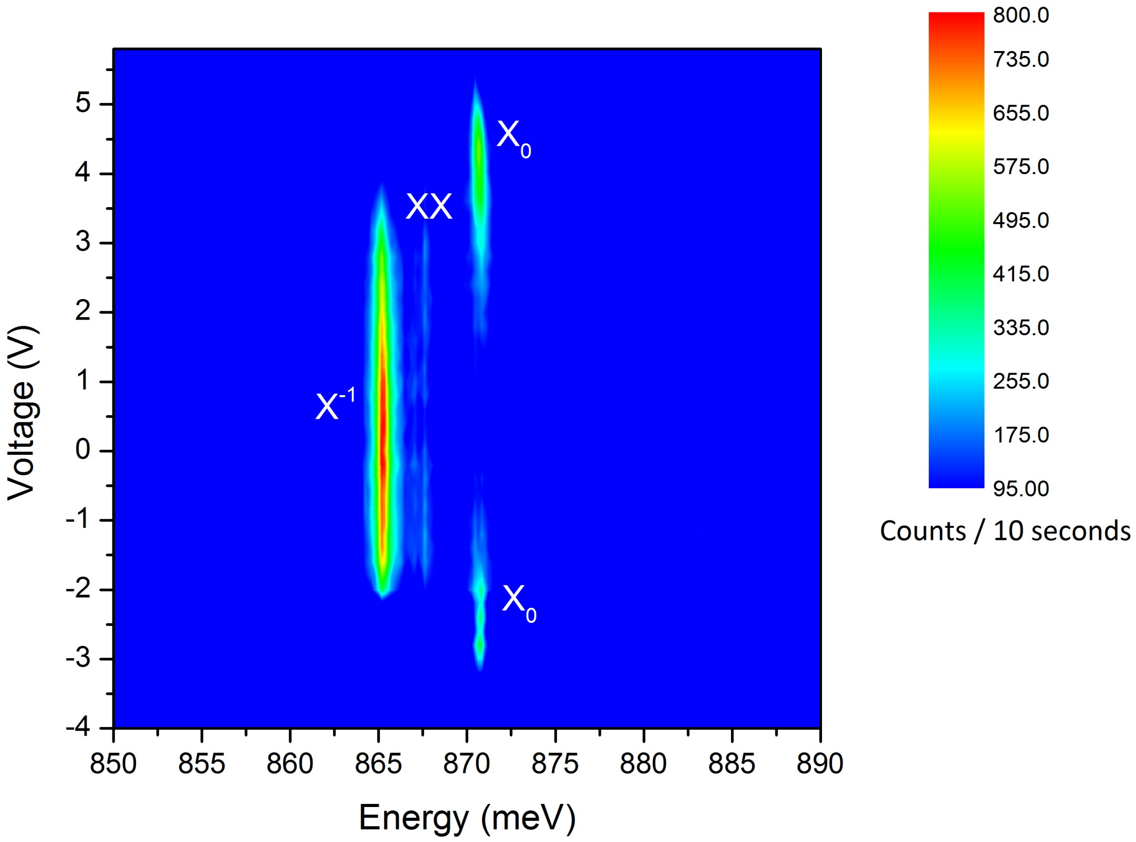

Figure 5.13: Photoluminescence spectra of a single dot as a function of lateral electric field intensity. Two opposite gates are set at a different bias. From lower to higher energy, the states are identified as X^{-1}, XX and the X^0, respectively. The states are identified by exchange splitting measurements and saturation behaviour at higher excitation powers.

Photoluminescence from a single dot as a function of voltage between opposite top gates is shown in Figure 5.13.

After a vertical field was first used to empty excess electrons from the dot so that the X^0 transition is clearly dominant, the exchange splitting of the exciton was measured as a function of lateral field. As the voltage between the opposite top gates is increased, the oscillator strength of the transition is reduced and the exchange splitting is decreased. Reductions in the exchange splitting of over 40% were achieved, as shown in Figure 5.14. However, this method of reducing the exchange splitting entirely is not practical. If the electron and hole are sufficiently separated to achieve a zero exchange splitting, the oscillator strength of the transition is necessarily zero and there is no photoluminescence.

5.7 Quadrapole electric field

One feature of the gated nanotemplate design is the possibility to generate unique localized fields which are only possible using a set of independent gates. One type of these unique configurations is the quadrapole field. In principle, a quadrapole field has the ability to correct the asymmetry of the confining potential of most dots.

The symmetry of the product of electron and hole wavefunctions is intimately related to the electron-hole exchange interaction, where

$$\Delta E_X \propto \iiint_{\infty} |\Phi_e|^2 \cdot |\Phi_h|^2 \, dx \, dy \, dz \tag{5.5}$$

where ΔE_X is the exchange splitting, Φ_e is the electron wavefunction and Φ_h is the hole wavefunction.

The change in the exchange splitting is proportional to the symmetry of the product of the electron and hole wavefunctions. The overlap of the electron and hole wavefunctions can potentially be tuned such that the integral vanishes and ΔE_X is zero. As the quadrapole field is increased, the electron and hole wavefunctions are elongated perpendicularly to each other. Depending on the sign of the quadrapole field, the exchange splitting can be increased or reduced by compensating for the inherent asymmetry of the dot. At a specific quadrapole field, measurements of the exchange splitting should indicate degenerate exciton states, and therefore the possibility to generate polarization-entangled photons.

A quadrapole field can be produced by applying a negative bias to two opposite top gates of the pyramid and applying a positive bias to the remaining two gates. The charge state of the dot changes as a function of the quadrapole field strength. A compensating vertical field was used to maintain a charge-neutral state as excess electrons from the wetting layer are repelled from the dot. The possibility to tune the exchange splitting through zero can be shown by a reversal of the phase of the exchange splitting as a function of wave plate angle. A reversal of this phase, and thus control over the geometry of the confining potential of the dot, was achieved and is shown in Figure 5.15. The functions are not exactly sinusoidal due to the dominance of photoluminescence transition from the lower energy X^0 state.

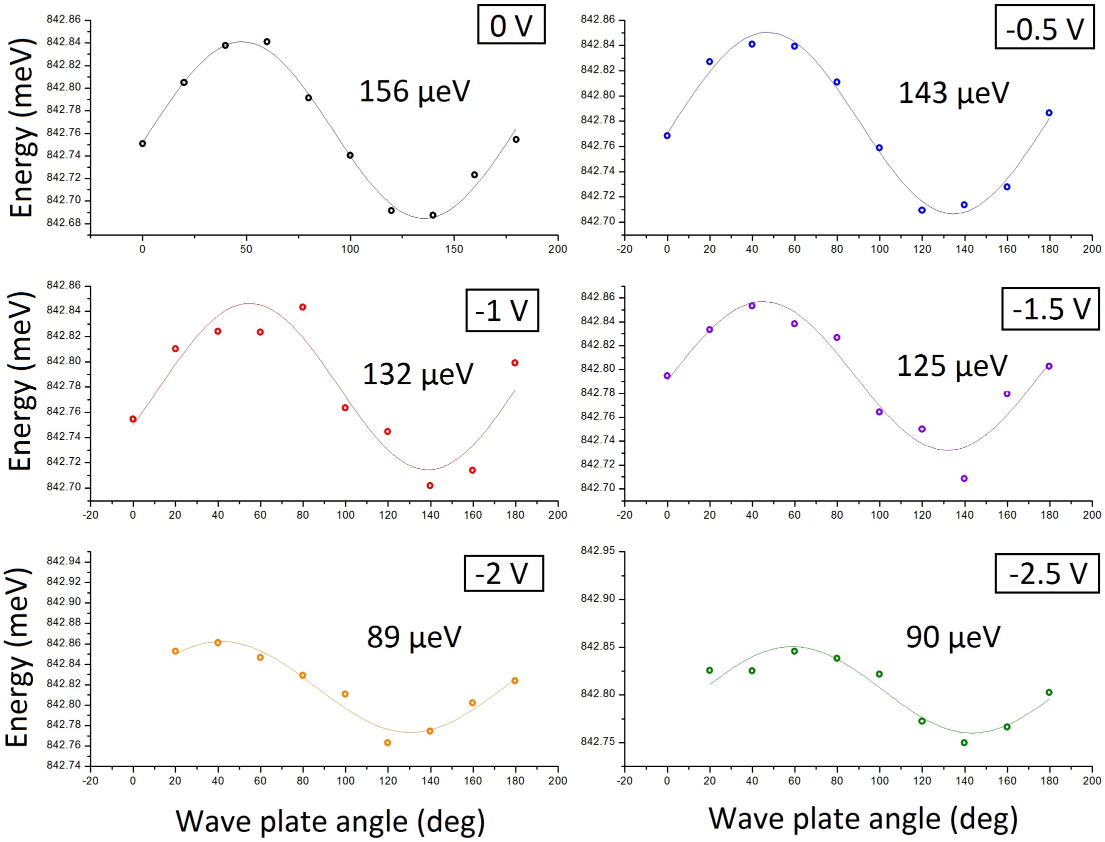

Figure 5.14: Emission peak energy as a function of wave plate angle for increasing lateral electric fields. At zero lateral field, the exchange splitting is about 156μeV. Increasing the voltage of opposite top gates reduces the exchange splitting of the exciton is to about 90μeV. The decreasing recombination rate makes it difficult to measure the exchange splitting at higher lateral fields.

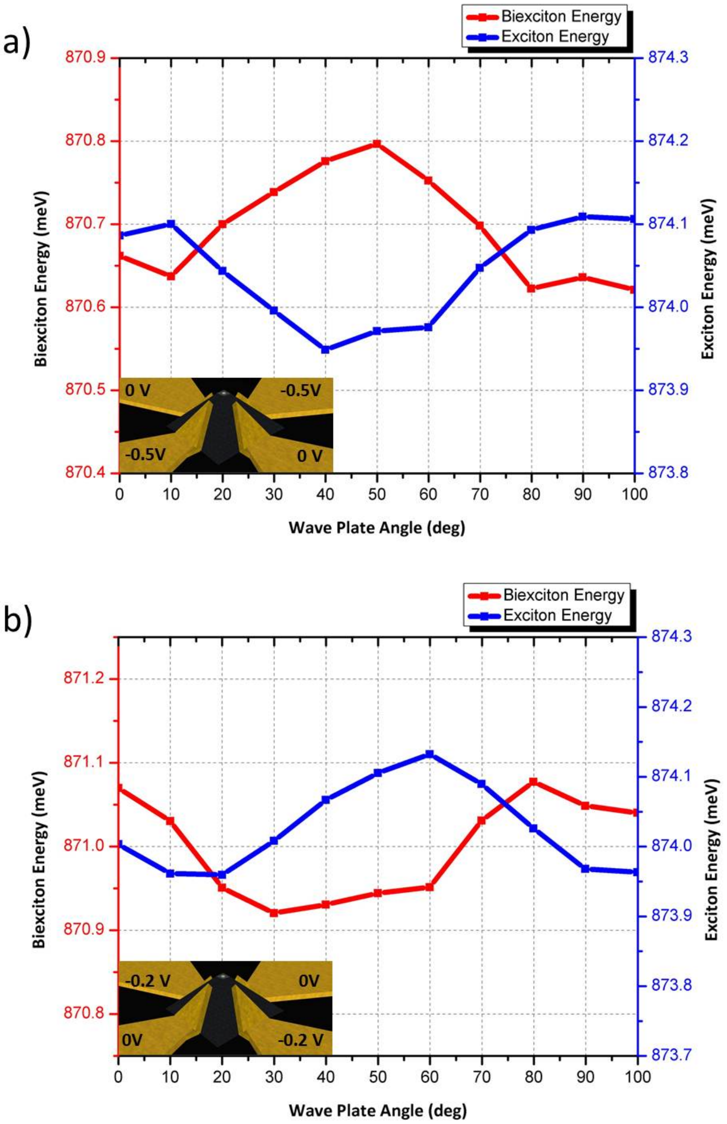

Figure 5.15: The reversal of the phase of the exchange splitting as a function of quadrapole field strength. The plot in (a) shows the exchange splitting of X^0 and XX with two gates set at -0.5V. The plot in (b) shows the exchange splitting of X^0 and XX with the two other gates set at -0.2V. This reversal suggests that the exchange splitting of the exciton can be tuned through zero.

5.8 Chapter summary

In summary, a gating strategy enabling local vertical and lateral electric field generation was successfully implemented in compatibility with the pyramidal nanotemplate. Current-voltage characteristics were measured and demonstrate good metal-semiconductor interfaces with slight variations in leakage current with different gates.

Vertical electric fields across a quantum dot were shown to control the charge state of the dot. A voltage between opposite top gates created a lateral electric field across single dots showing a clear reduction in the exchange splitting, as well as influence on the charge state due to additional vertical electric field components from the top gates. Quadrapole electric field configurations were created using oppositely-biased adjacent gates. The exchange splitting of the exciton and biexciton are reversed as the quadrapole field orientation is flipped. This suggests that confining potential of a single dot can be controlled, and the exchange splitting of the X^0 state can be tuned through zero.

Chapter 6

Magnetophotoluminescence spectroscopy of single InAs/InP dots in pyramidal nanotemplates

6.1 Introduction

At present, quantum dots have been used in a variety of applications such as solar cells, lasers and as labels for imaging of organic matter, all of which use the broad photoluminescence of an ensemble of dots. Potential applications such as quantum computing and spin-selective single photon detectors, however, require a combination of single dot isolation techniques and control over the spin properties of single dots. The operation of these spin-based quantum information devices depends on the behaviour of the confined electrons and holes in the presence of a magnetic field. Hence, the magnetophotoluminescence of dots can provide clues to the excitonic fine-structure of dots[66]. Through the control over the physical properties of single dots provided by the pyramidal nanotemplate, the spin-properties of dots may also be engineered.

This chapter explores the magnetophotoluminescence spectra of single InAs/InP quantum dots embedded in pyramidal nanotemplates in order to provide clues to their physical size, shape and fine structure. The dispersion of the s, p and d states as a function of magnetic field intensity is discussed. A new sample design and the experimental apparatus used for high magnetic field photoluminescence spectroscopy are described. The g-factor and diamagnetic coefficients for both the X^0 and X^{-1} states are calculated from the magnetophotoluminescence of single dots. Polarization-resolved spectroscopy is used to identify the spin configurations of the exciton states.

6.2 Magnetophotoluminescence spectroscopy of single InAs/InP dots

High-field magnetospectroscopy of single quantum dots requires a cryostat positioned a the centre of a superconducting magnet or electromagnet. Collaborations with the "Laboratoire Nationale des Champs Magnétiques Intenses" (LNCMI) in Grenoble, France have provided access to a 14T bipolar superconducting magnet and a 28T electromagnet. The sample was mounted in a long metal dipstick probe placed at the centre of a cryogenically-cooled cryostat located at the centre of a magnet. The sample was held at a temperature of approximately 4.2K by immersion into liquid helium surrounded by a sheath of liquid nitrogen. The superconducting magnet itself also requires cryogenic cooling using liquid helium and nitrogen. The magnetic field was applied in the Faraday configuration(vertically). Due to the exclusive use of fibre-based optics inside the cryostat, the experimental configuration does not allow for observation of the sample once inside the probe.

Magnetophotoluminescence spectra of single dots in pyramids were measured using either the 14T superconducting magnet, or the 28T electromagnet for high field measurements. The laser beam was depolarized using an active polarization modulator in order to avoid field-dependent rotations of the photoluminescence polarization due to the Faraday effect. A continuous wave He-Ne laser was used as the laser source. The beam was focused into a single mode optical fibre, guided through one arm of a y-spliced optical fibre, and directed perpendicular to the sample surface. The photoluminescence was obtained through the same fibre before being diverted into the other arm of the fibre. The photoluminescence is then collimated into free-space, and focused on the spectrometer slit. The collimating lens has a focal length of 100mm with an anti-reflection coating for wavelengths in the range of 1050nm-1620nm.

To measure the photoluminescence, a 0.25m spectrometer in combination with an InGaAs detector was used. The InGaAs spectrometer uses a 600 lines/mm grating blazed at 1.2μm with a spectral resolution of about 0.11nm. The integration time for the measurement of photoluminescence spectra was 10 seconds, unless stated otherwise. The emission spectra of more than fifty different single InAs/InP quantum dots on ungated InP pyramids were measured in magnetic fields up to 27.7T. Measurements were taken in 0.3T increments of field intensity increased at a rate of about 3T per minute up to 27.7T.

To move around the sample, the sample is placed on a stack of three Attocube® piezoelectric actuators. Two of these actuators are used to move parallel the sample

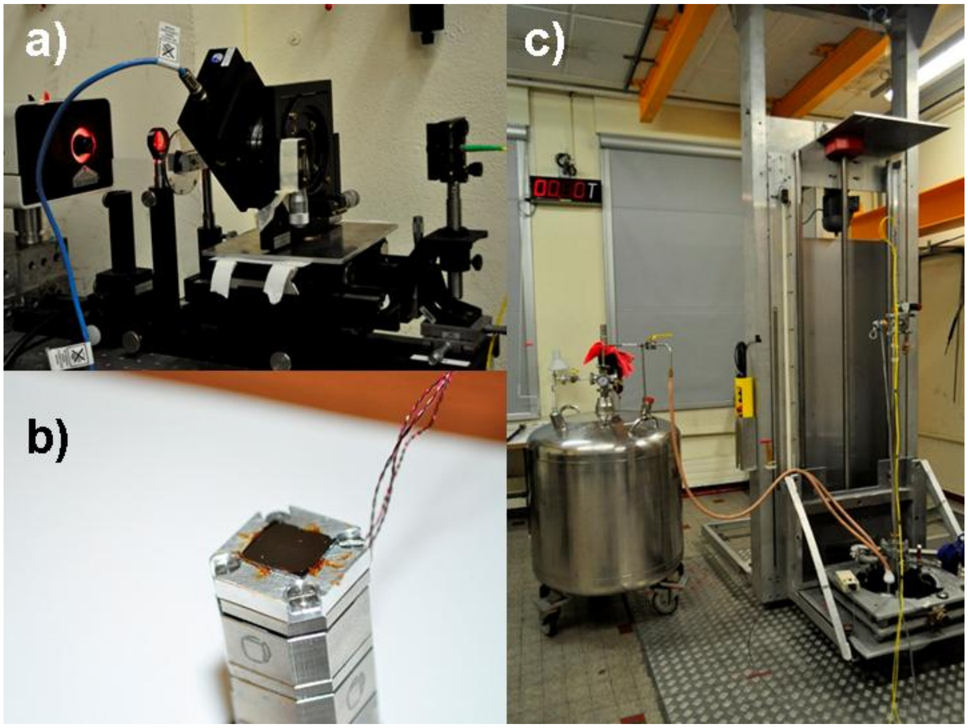

Figure 6.1: Photograph of (a) the laser source being passed through a polarization modulator and directed into an optical fibre, (b) a sample mounted to a stack of three Attocube® positioners, and (c) the 28T electromagnet with an inserted dipstick probe. The magnet is located beneath the floor.

surface. A third Attocube® actuator is used move the sample perpendicular to the laser beam, effectively adjusting the focus of the incident laser on the sample. GE low temperature varnish is used to attach the sample to the Attocube® stages. Navigating the sample despite no viewing system is possible by ensuring an alignment between the array of pyramids and Attocube® positioner axes. Photographs of a mounted sample and the laboratory apparatus are shown in Figure 6.1.

The gated samples described in the previous chapter are not ideal for use in such a cryostat. The low dot density and lack of sufficient alignment structures make it difficult to navigate the sample without an imaging system. A new sample was designed and grown by Dr. Dan Dalacu, which was designed to produce a dense array of pyramids with an array of cross-shaped ridges between each pyramid, as shown in Figure 6.2. Additional horizontal and vertical InP ridges were grown to help align the laser spot to the array of dots. The photoluminescence of these ridges revealed distinct peaks corresponding to their monolayer fluctuations of height. Schematics of the design can be seen in Figures 6.3, 6.4 and 6.5.

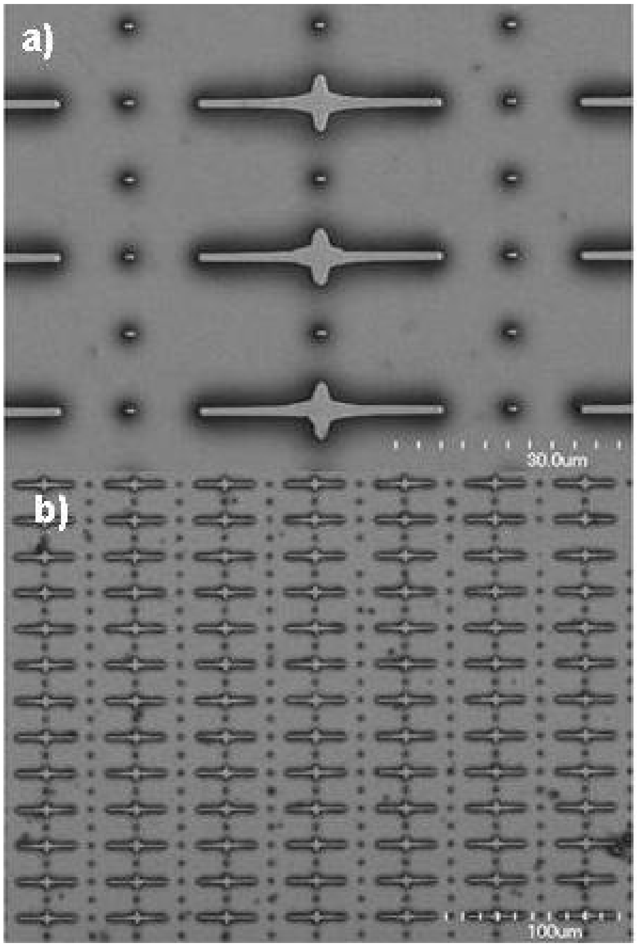

Figure 6.2: SEM micrographs of (a) pyramids and crosses showing elongated pyramids due to larger InP capping to provide better dot confinement and hence brighter photoluminescence, and (b) the array of pyramids and cross-shaped ridges. The small dots are the pyramids.

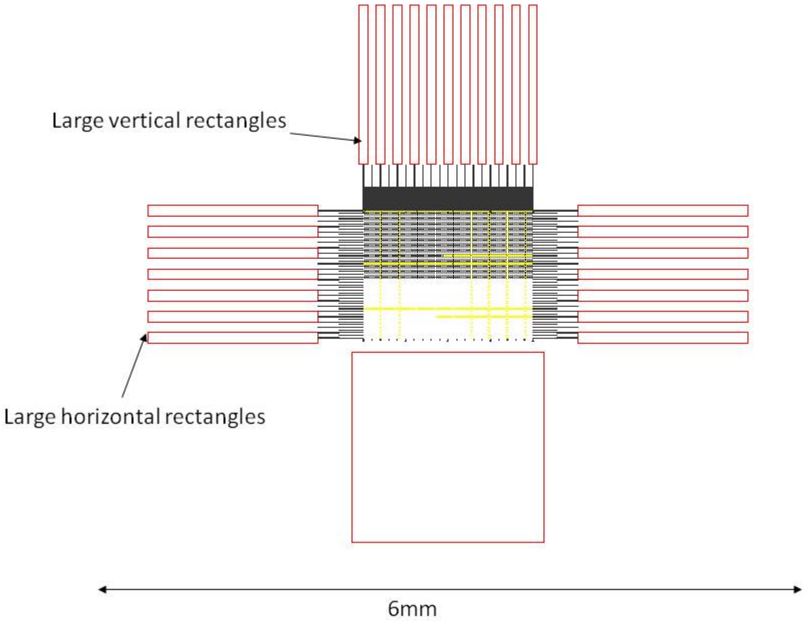

Figure 6.3: Schematic of the entire sample with a dense array of pyramids. The large alignment structures are outlined in red. The dense array of pyramids and crosses is located at the centre.

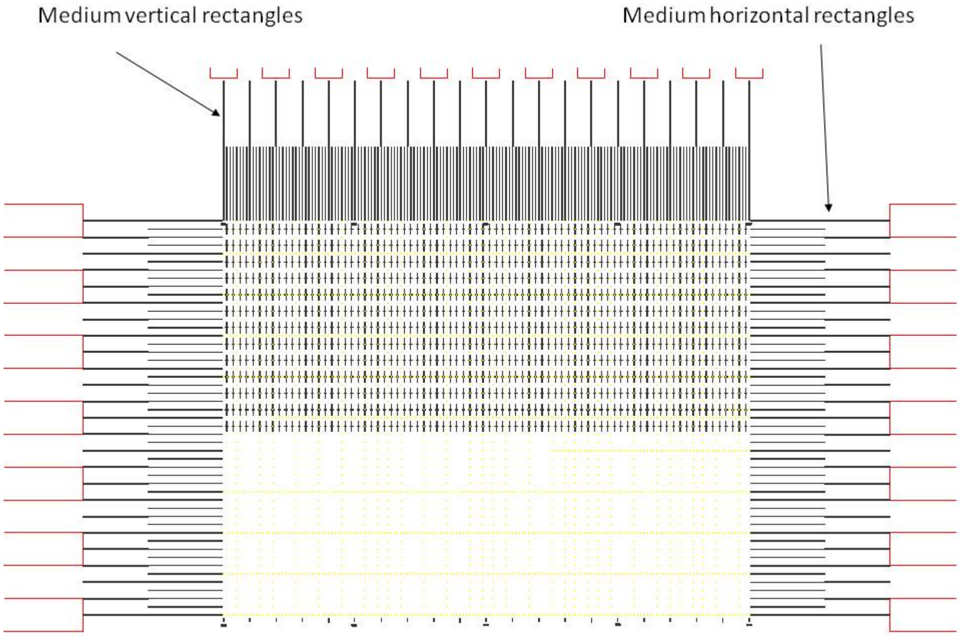

Figure 6.4: Schematic of the medium alignment structures of the sample. The progressively finer vertical and horizontal alignment structures are used for navigating and positioning the laser spot.

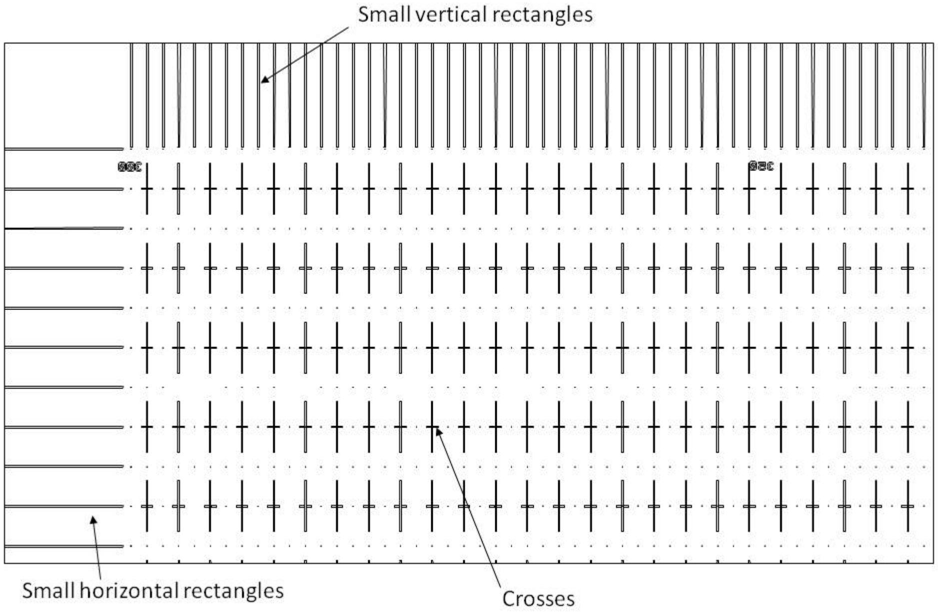

Figure 6.5: Schematic of the dense array of pyramids and crosses. The fine alignment structures are aligned with the array of pyramids.

Photoluminescence spectra of the sample suggest most pyramids contain single dots which emit photons with energies in the 800-870 meV range. Single, resolution-limited peaks at low laser power suggest many pyramids contain single dots as shown in Figure 6.6. At low power and low magnetic field, the dots can be excited into the X^{-1} or the X^0 states. The X^0 state appears at a few meVs above the X^{-1} state. With increasing laser power, electrons in the dot can be excited into the p and d states as shown in Figure 6.7. The energy gap from the s to p states is consistently around 20meV and shows no clear dependence on ground state emission energy. Magnetophotoluminescence spectra of some of the single dots are shown in Figure 6.8 at low and high pump powers.

6.3 Excitonic g-factor and diamagnetic shift

Much like the electronic states of conventional atoms, the exciton states in ideal dots are doubly degenerate due to the two possible spin configurations for each state. This is often called the Kramers degeneracy. In the presence of a magnetic field, this degeneracy is broken and the energy splitting between the two states increases as a function of the magnetic field intensity.

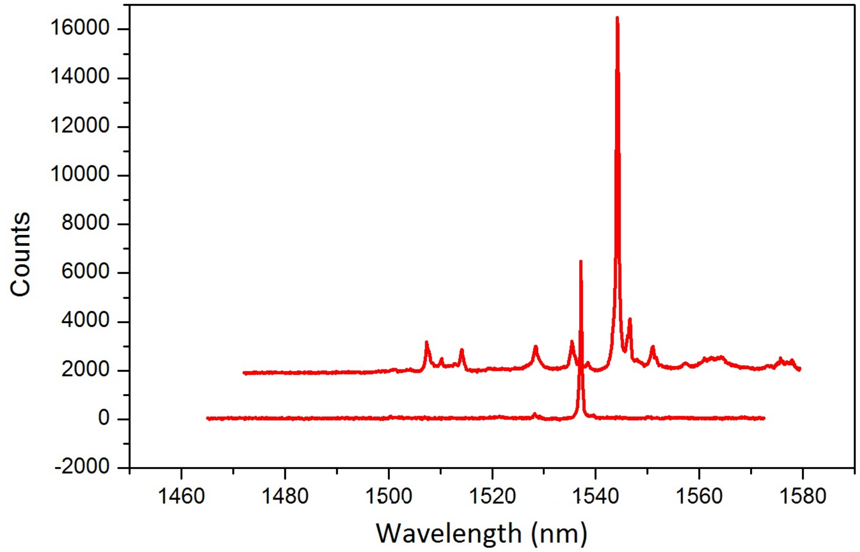

Figure 6.6: Photoluminescence spectra of a single dot in a pyramid at low (lower curve) and high power (higher curve). The signal-to-noise ratio of the photoluminescence spectra of the dots is extremely good. The predominance of a single peak suggests there is only a single dot in each pyramid. The extra peaks at higher laser power are attributed to the excitation of nearby dots, transitions involving the p-states, biexciton, and other charged states.

The energy state dispersion in a magnetic field can be described by the model,

$$E_{\pm} = E_0 \pm g_{ex}\mu_B B + \gamma B^2 \tag{6.1}$$

where g_{ex} is the exciton g-factor, B is the magnetic field, E_0 is the zero-field energy, μ_B is the Bohr magneton, and γ is the diamagnetic coefficient. The g-factor g_{ex} describes the linear splitting between the two states, while the diamagnetic coefficient γ describes the quadratic dispersion of the states.

The g-factor of the X^0 and X^{-1} states is measured using the formula,

$$g_{ex} = \frac{E(\sigma_+) - E(\sigma_-)}{\mu_B B} \tag{6.2}$$

where μ_B is the Bohr magneton, B is the magnetic field ,and $E(\sigma_+)$ and $E(\sigma_-)$ represent the right and left circular polarized states, respectively.

The magnetic field was slowly increased to 27.7T, where the linear dispersion be-

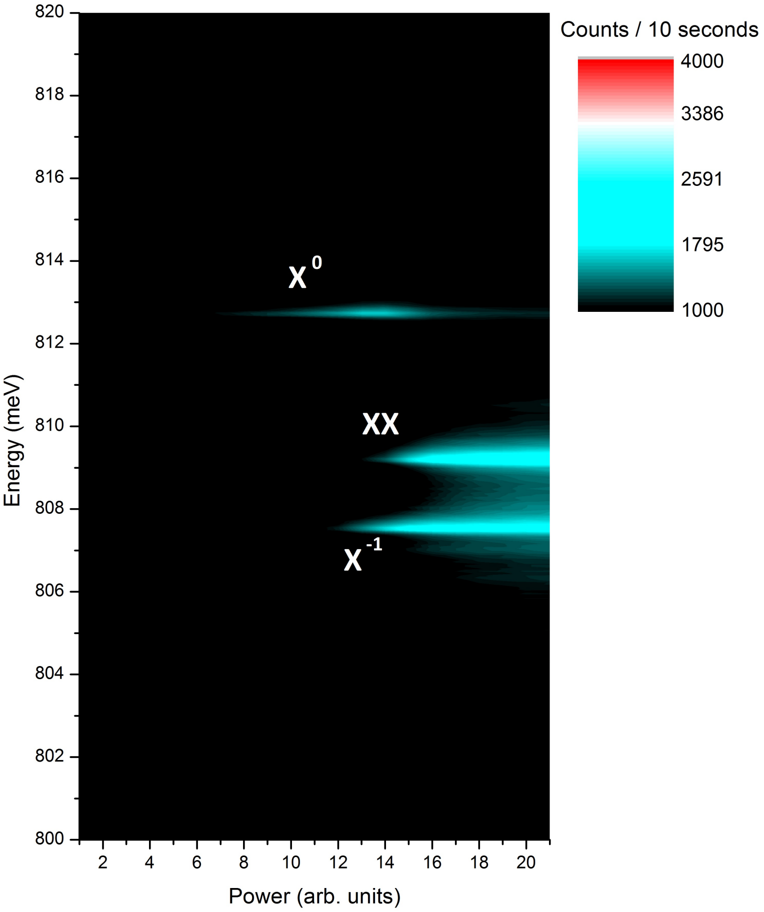

Figure 6.7: Photoluminescence spectra of a single dot in a pyramid as a function of laser power. The dot is initially excited into the X^0 state at low laser power and saturates with higher power. With increasing laser power, more carriers are excited and the XX and X^{-1} states can be populated.

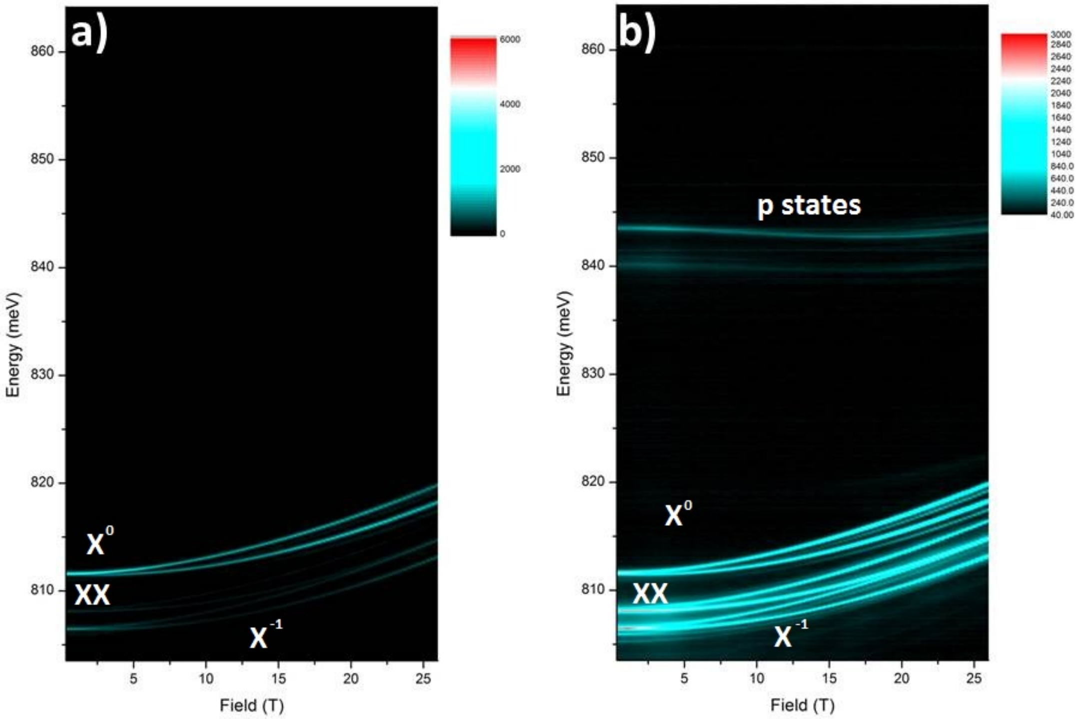

Figure 6.8: Photoluminescence spectra as a function of magnetic field at (a) low laser power and (b) high laser power. In this case, the X^0 state is very clear and dominant at low excitation powers. At higher power, the X^{-1} and XX states are also occupied. The similar dispersion of the XX, X^0 and X^{-1} states indicate that all states have approximately the same g-factor.

tween the right and left circularly polarized states was recorded in order to calculate the g-factor. The g-factor of the X^{-1} and X^0 states was found to increase as an approximately linear function of emission energy as shown in Figure 6.9. The g-factors ranged from around -1.6 to -0.4 for the dots measured. This result is in agreement with previous work [67], but opposite in sign with other work on the subject[68]. The g-factors of both X^{-1} and X^0 states are very similar for every dot. As the ground state X^0 emission energy increases, the g-factor increases linearly. Since the wavelength of the emitted photons from a dot depends on its size, the g-factor of a single dot can be tuned by controlling the surface area of the plateau of the pyramid upon which the quantum dot is grown.

Once the g-factor is measured, the diamagnetic shift can be calculated by rearrang-

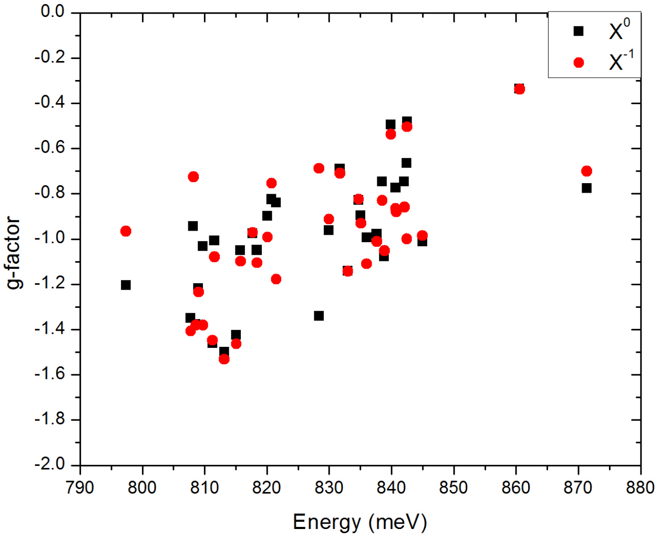

Figure 6.9: Exciton and charged exciton g-factors as a function of ground state emission energy. The exciton g-factor clearly becomes less negative with increasing emission energy. Both the X^{-1} and X^0 g-factors are similar in the majority of quantum dots examined. Error bars are too small and are not shown for clarity.

ing Equation 6.1, and can be expressed as

$$\gamma_D = \frac{E_{av} - E_0}{B^2}, \tag{6.3}$$

where γ_D is the diamagnetic coefficient that corresponds to the quadratic dispersion of the states.

The diamagnetic coefficient (γ_D) was calculated for both X^0 and X^{-1} states using the measured g-factor up to 27.7T. The diamagnetic coefficient did not vary with X^0 emission energy. The small differences in diamagnetic coefficients between each dot suggest that the shape of the dots is fairly homogeneous. Similar diamagnetic coefficients were found for both the X^0 and X^{-1} states (see Figure 6.10). This coefficient varies from a value of 10-14 μeV/T^2, indicating dot diameters of roughly 30-40nm[69]. The g-factor was also plotted as a function of the diamagnetic shift, showing a strong linear correlation for both X^0 and X^{-1} states, as shown in Figure 6.11

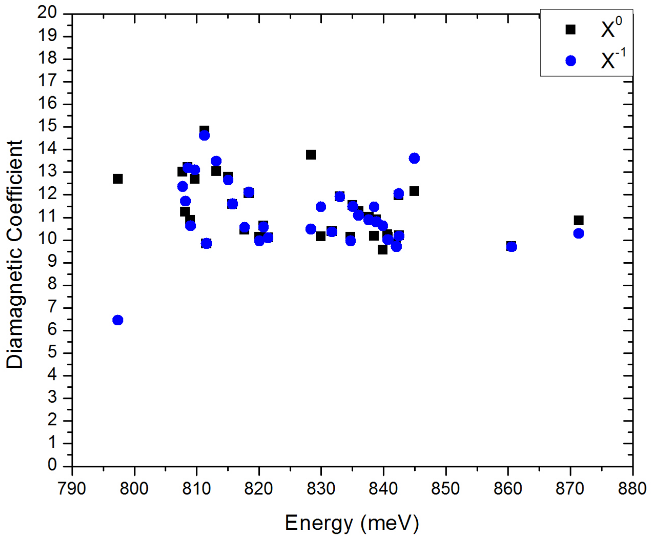

Figure 6.10: Diamagnetic coefficient as function of the ground state emission energy of the X^0 and X^{-1} states. Error bars are too small and are not shown for clarity.

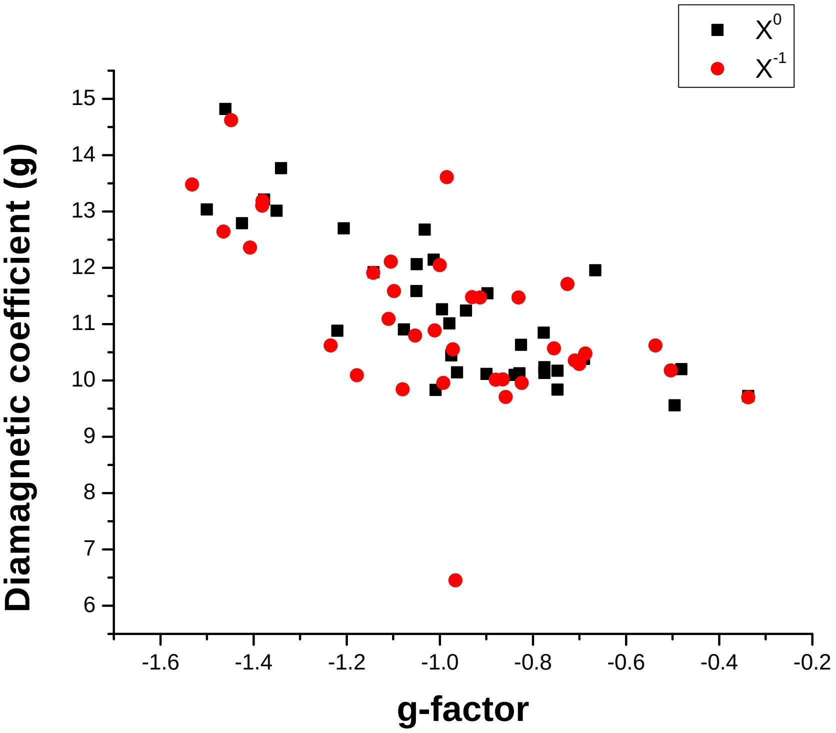

Figure 6.11: The g-factor of the X^0 and X^{-1} states plotted as a function of the diamagnetic coefficient. Error bars are too small and are not shown for clarity.

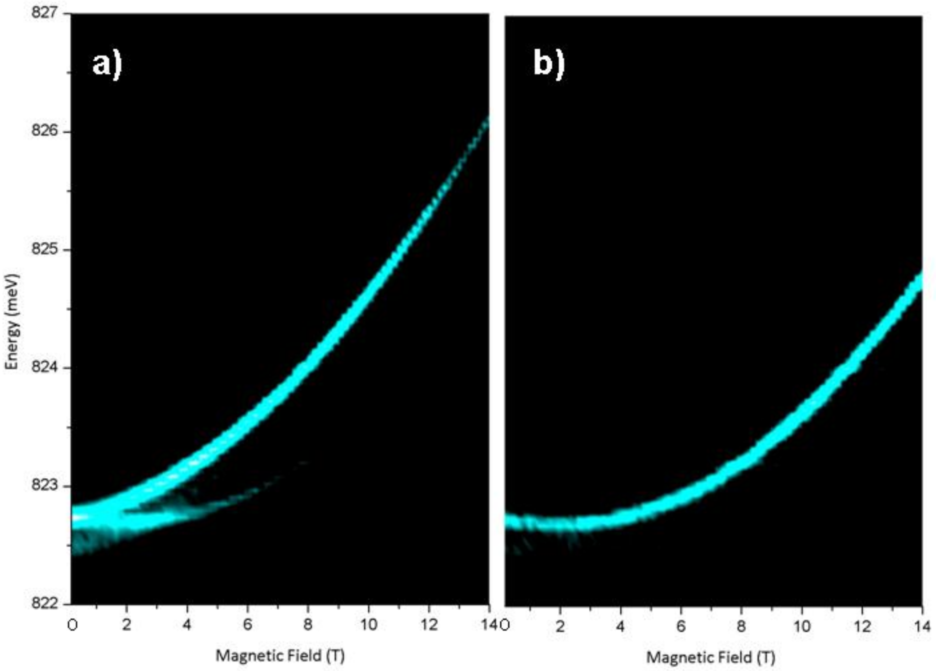

Figure 6.12: Polarization-resolved magnetophotoluminescence spectra of a single dot. The emission spectra from the (a) σ_- and (b) σ_+ states are isolated. Turquoise colour indicates photoluminescence.

6.4 Polarization-resolved spectroscopy

The doubly degenerate states of a quantum dot can be split using a magnetic field in order to obtain information regarding the spin relaxation mechanisms[70]. In the presence of a magnetic field, the Zeeman effect splits each doubly degenerate state into two distinct states (σ_- and σ_+) emitting left and right circularly polarized photons relative to the vertical magnetic field, respectively. The photoluminescence from each dot was passed through a quarter-wave plate in order to convert the circular polarized light to linearly polarized light. A Glan-Thompson polarizer and a half-wave plate were then used to identify each transition by linear polarization. The polarization-resolved magnetophotoluminescence spectra shown in Figures 6.12 demonstrate the circular polarization of the emitted photons from the two states. Due to perturbations in the optical fibre, the polarization of the emitted photons slowly changes over the measurement time. The ellipticity of the measured polarization can be corrected using the quarter-wave plate after each measurement.

6.5 Chapter summary

In summary, knowledge of the shape, size, g-factor and diamagnetic shift of single dots is crucial in order to realize possible quantum information applications. This chapter has explored the magneto-optical properties of single InAs/InP quantum dots embedded in ungated pyramidal nanotemplates in magnetic fields. A new sample design was devised and implemented successfully to measure the magnetophotoluminescence of many single dots. No significant difference between the g-factors of the X^{-1} or the X^0 states was found in most dots. The g-factor of the dots was determined to range from -1.6 to -0.4 and correlated to the dot emission energy. The g-factors of both X^{-1} and X^0 states show a positive linear trend with ground state emission energy ranging from 800-870 meV. Through control of the emitted photon wavelength using the nanotemplate, single dot g-factors can be engineered. The diamagnetic shift shows no dependence on emission energy for either X^{-1} and X^0 states, ranging from 10-14 μeV/T^2, suggesting a fairly consistent dot shape and size of about 30-40nm.

Chapter 7

Conclusions

7.1 Conclusions

The research objectives accomplished in this thesis were:

- Demonstration of control over the charged state of a single InAs/InP quantum dot in a pyramidal nanotemplate using simultaneous lateral and vertical electrostatic gating.
- Measurement of the exchange splitting of the X^0, X^{-1} and XX states.
- Flipping of the exchange splitting of the X^0 using a quadrapole electric field configuration.
- Improved measurements of the g-factor and diamagnetic shift of single InAs/InP quantum dots in pyramidal nanotemplates

The work in this thesis reflects the utility of the pyramidal nanotemplate, where the optical and electronic properties of single quantum dots can be tuned. Single InAs/InP dots can be tailored to emit exactly at the desired wavelength for minimum attenuation in optical fibre while being precisely isolated and positioned. The unique nanotemplate fabrication procedure has demonstrated the greatest amount of control over the physical, electronic and optical properties of a single self-assembled quantum dot. The ability to simultaneously apply a localized vertical and lateral electric field to a single pre-positioned quantum dot was demonstrated for the first time. In addition, reversible control of the exciton exchange splitting using a quadrapole electric field was also demonstrated for the first time.

With the addition of four laterally-positioned gates on the sidewalls of the pyramidal nanotemplate, applied electric fields have allowed precise control over the charged state of the dot. The charging spectra for vertical and lateral electric field configurations were measured. In general, due to the natural asymmetry of most dots, exchange splittings of 150-250μeV for the X^0 state were measured. A zero exchange splitting was confirmed for the X^{-1} state. The exchange splitting of the XX state was opposite in sign to that of the X^0 state as expected. A vertical electric field was used to control the charged state of a single dot. A lateral electric field configuration was used to reduce the exchange splitting of the X^0 state. A quadrapole electric field configuration was successfully used to reverse the exchange splitting of the X^0 and XX states with a reversal of the quadrapole field geometry. This suggests that localized electric fields can be used to reversibly tune the exchange splitting of the X^0 state through zero.

Magnetophotoluminescence spectroscopy of many InAs/InP dots in pyramids revealed a linear dependent of the g-factor with emission energy. The relatively constant diamagnetic coefficient of the X and X^{-1} states suggest a consistent shape for most the dots studied. The g-factor was also shown to depend linearly on the diamagnetic coefficient.

The ability to reversibly control the exciton exchange splitting of a single quantum dot provides a scalable route to controlling the entanglement of on-demand photon pairs using solid state fabrication processes. The wavelength of the entangled photons created using the InAs/InP quantum dot system can be tuned for minimum attenuation through standard optical fibre, enabling the long-distance transmission of entangled photons for future applications in quantum cryptography and other quantum information devices.

7.2 Future work: Gated dots in photonic crystal cavities

With the ability to tune the exchange splitting of a quantum dot through zero, it is possible to generate polarization-entangled photon pairs from the two intermediate X^0 states in the biexciton cascade. However, the problem with quantum dots as isolated structures is that the radiative lifetime of the exciton can be undesirably long, reducing the photon emission efficiency from dot. By confining a resonant electromagnetic field around a quantum dot, the spontaneous emission of the dot can be greatly enhanced. This effect is called the Purcell effect. The Purcell factor, which determines the level of enhancement is

$$F_P = \frac{3}{4\pi^2}\left(\frac{\lambda}{n}\right)^3\left(\frac{Q}{V}\right), \tag{7.1}$$

where F_P is the Purcell factor, λ is the wavelength of the cavity-supported mode, n is the index of refraction of the cavity material , Q is quality factor and V is mode volume of the cavity. The enhancement of the spontaneous emission of the dot is dependent on a large quality factor and a small mode volume.

Photonic crystal cavities are enclosed semiconductor structures with a matrix of etched holes which change the effective refractive index of the material. Two-dimensional photonic crystal cavities are planar structures which primarily emit photons at a direction normal to the cavity plane and can be post-fabricated around quantum dots. At the centre of the cavity, there is a defect in the etched lattice, resulting in the confinement of light at the centre.

The next step towards realizing a scalable architecture for entangled photon pair generation is to place a gated quantum dot inside a two-dimensional photonic crystal cavity. Such a cavity design has been previously realized by Dr. Dan Dalacu[71] and is shown in Figure 7.1. The cavity enhances the spontaneous emission of the dot if the dot is placed at the centre of the cavity and emits photons with the same energy as the cavity-supported mode. A significant challenge with the incorporation of a single dot in a cavity is the difficulty in positioning a single dot at the centre of the cavity mode. A simple strategy is to simply fabricate an array of cavities atop a substrate of quantum dots and to rely on the chance there exists a single dot in the right position emitting at the same wavelength as the cavity mode. If one fabricates a sufficiently large array of cavities, there exists a chance of this occurring enough despite the low yield of good samples. This strategy may be sufficient for proof-of-principle experiments, but not for the fabrication of a scalable system.

Using the site-selective growth techniques outlined in this thesis, a single dot can not only be precisely positioned near the centre of the cavity, but also engineered to emit photons with an energy in resonance with the cavity mode. Post-fabrication tuning of photonic crystal cavities has also been demonstrated using nitrogen deposition and wet etching techniques to tune the cavity in resonance with the dot[72]. It is also important to maintain a high quality factor in a gated cavity structure. By tuning the exchange splitting to zero, and placing a resonant dot at the the centre of a photonic crystal cavity, an on-demand source of entangled photon pairs can be realized.

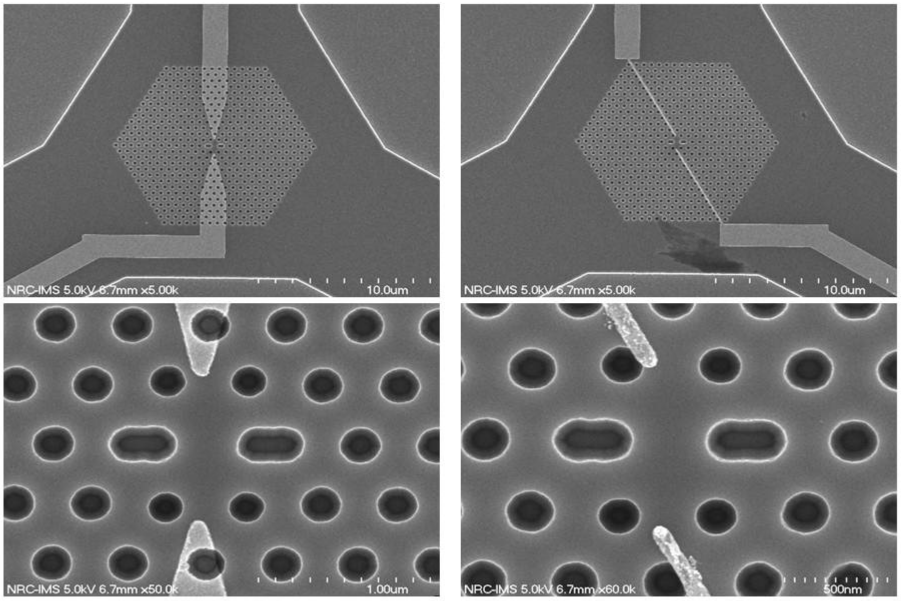

Figure 7.1: SEM image of a gated photonic crystal cavity. Two gates are designed to control the charge state of the quantum dot, which is located in the centre of the cavity.

7.3 Future work: Gated dots in magnetic fields

As described in the previous chapter, it is highly desirable to control the charged state of the quantum dot. The magnetophotoluminescence of single InAs/InP quantum dots reveals a rich family of these charged states. To further probe the spin properties of specific charge states of a quantum dot (such as X^{-1}, X^{0} and X^{+1}), measurements can be made while controlling the local electric fields in conjunction with an external magnetic field.

Efforts to measure the magnetophotoluminescence of a gated dot have been made in this thesis. The gated samples used for the manipulation of the exchange splitting in Chapter Five were modified for use in a cryostat in a high magnetic field at the "Laboratoire National des Champs Magnétiques Intenses", as shown in Figure 7.2. The pins on the chip mount were bend outwards to connect to wires traveling up the dipstick probe to the voltage source. Wires were then soldered to the pins on the sample mount. The sample mount was fixed to a plastic square spacer using GE varnish. The plastic spacer was fixed to the Attocube® piezoelectric positioners. This spacer acted as an insulator to prevent the electrical shorting of the gates to the Attocube® stage.

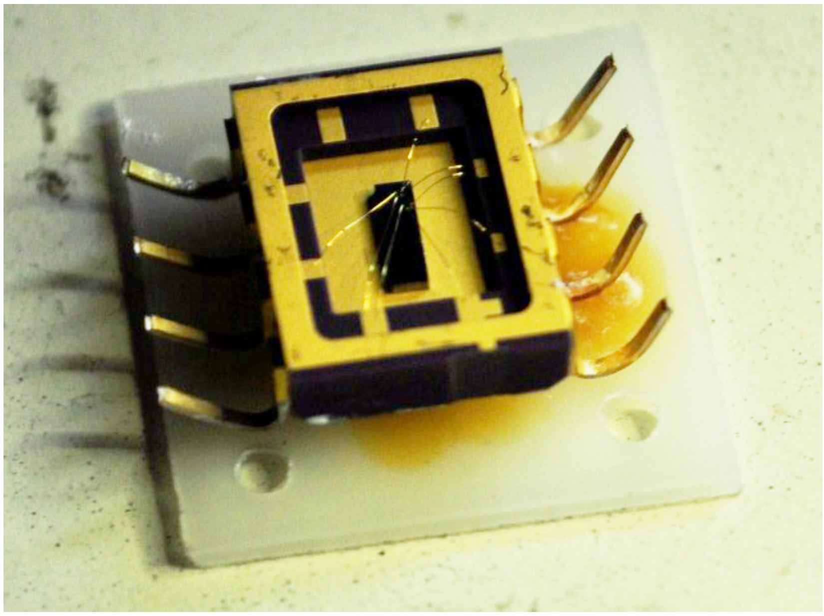

Figure 7.2: Gated sample on a plastic spacer. The pins have been bent outward to fit inside the dipstick probe and to facilitate the soldering of the connecting wires.

While mounting the sample inside the probe, the gated sample was kept grounded to reduce the risk of electrical shorting through the substrate.

The application of both magnetic and local electric fields to a quantum dot was non-trivial. The probe for the electromagnet is wired to the gates on the pyramid, which exposes the gated pyramid to high voltage spikes while soldering the wires to the pin contacts. The gated pyramid is sensitive to static electricity and can be destroyed without proper electrical grounding within the probe. The second issue is the difficulty involved in navigating the sample without an imaging system to view the sample. There were no vertical or horizontal alignment marks which photoluminesce to locate the position of the gated pyramid. The density of pyramids is also much lower, making it difficult to navigate an array of pyramids. A third issue arises from the increased difficulty to align the gated samples to the axes of motion of the piezoelectric positioners. In order to provide some alignment markers, cleaved chips containing vertical and horizontal alignment marks were placed next to gated pyramid samples using silver epoxy in order to help with locating the sample on the chip mount, as shown in Figure 7.3.

In practice, the pyramids were located by the contrast in photoluminescence from the gold gates and bond pads to the exposed InP substrate at high laser powers. The InP substrate photoluminesces slightly at high optical powers in contrast to the lack of

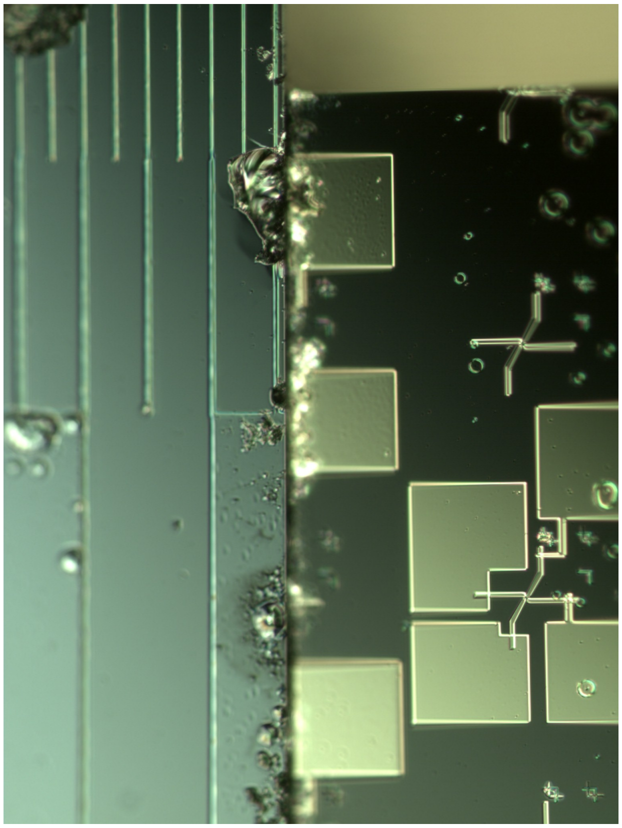

Figure 7.3: Optical micrograph of a gated sample beside a reference sample with alignment marks. The gold on the sample to the right reflects the pump laser and results in no photoluminescence of the InP substrate, which helps to distinguish surface features for effective navigation around the sample.

photoluminescence from gold gates due to reflection. Using this combination of electric and magnetic field sources, the spin properties of each charged state of a single dot can be selectively mapped.

7.4 Statement of work

The research described in this Thesis has relied on years of experience and development of the experimental methods towards the fabrication and measurement of quantum dots. This effort is led by Dr. Robin Williams and Dr. Dan Dalacu. The work done in this thesis comprises:

- Measurements of the photoluminescence of single InAs/InP dots embedded in pyramidal nanotemplates as a function of optical pump power, and electric field

- Measurements of the exciton, biexciton, and charged exciton exchange splittings
- Optimization of the data acquisition software
- I-V characteristics of the gated pyramid
- All optical and some SEM micrographs
- Magnetophotoluminescence spectroscopy of dots in pyramidal nanotemplates
- Development of the gating configuration within the dip-stick probe
- Optimization of the optical spectroscopy setup in the laboratory

The development of the quantum dot growth recipe, sample design, and laboratory apparatus were done by Dr. Dan Dalacu. The motivation for the quadrapole gating configuration was led by Dr. Robin Williams and Dr. Eugene Kadantsev. The algorithm for fitting the photoluminescence peaks to measure the exchange splitting was developed by Dr. Vera Sazonova.

Bibliography

[1] M.M.J. Treacy, T.W. Ebbesen, and J.M. Gibson. Exceptionally high Young's modulus observed for individual carbon nanotubes. *Nature Lett.*, 381:678–680, June 1996.

[2] Daniel Loss and David P. DiVincenzo. Quantum computation with quantum dots. *Physical Review A.*, 57:120–126, January 1998.

[3] E. Knill, R. LaFlamme, and G.J. Milburn. A scheme for efficient quantum computation with linear optics. *Nature*, 409:46–52, November 2000.

[4] A.K. Geim and K.S. Novoselov. The rise of graphene. *Nature Materials.*, 6:183–191, 2007.

[5] A. Ekimov, A. Efros, and A. Onushchenko. Quantum size effect in semiconductor microcrystals. *Solid State Communications*, 56:921, 1985.

[6] Weidong Sheng and Jean-Pierre Leburton. Electron-hole alignment in InAs/GaAs self-assembled quantum dots: Effects of chemical composition and dot shape. *Phys. Rev. B.*, 63(161301), 2001.

[7] H. Drexler, D. Leonard, W. Hansen, J.P. Kotthaus, and P.M. Petroff. Spectroscopy of quantum levels in charge-tunable InGaAs quantum dots. *Phys. Rev. Lett.*, 73:2252–2255, 1994.

[8] A.J. Nozik. Quantum dot solar cells. *Physica E*, 14:115–120, 2002.

[9] R. Colin Johnson. MIT harvests heat with quantum dots to double battery lifetimes. *Smarter Technology*, 2009.

[10] X. Michalet, F.F. Pinaud, L.A. Bentolila, J.M. Tsay, S.Doose, J.J Li, G. Sundaresan, A.M. Wu, S.S. Gambhir, and S. Weiss. Quantum dots for live cells in vivo imaging and diagnostics. *Science*, 307(5709):538–544, January 2005.

[11] C. Santori, D. Fattal, J. Vuckovic, G. Solomon, and Y. Yamamoto. Indistinguishable photons from a single-photon device. *Nature*, 419(1):594–7, 2002.

[12] Robert J. Young, David J. P. Ellis, R. Mark Stevenson, Anthony J. Bennett, Paola Atkinson, Ken Cooper, David A. Ritchie, and Andrew J. Shields. Quantum-dot sources for single photons and entangled photon pairs. *Preceedings of the IEEE*, 95(9):1805–1814, September 2007.

[13] Karl Eberl. Quantum dots lasers. *Physics World*, pages 47–52, September 1997.

[14] P. Michler, A.Kiraz, C. Becher, W.V. Schoenfeld, P.M. Petroff, Lidong Zhang, E. Hu, and A. Imamoglu. A quantum dot single-photon turnstile device. *Science*, 290(5500):2282–2285, December 2000.

[15] R. M. Stevenson, R. J. Young, P. Atkinson, K. Cooper, D. A. Ritchie, and A. J. Shields. A semiconductor source of triggered entangled photon pairs. *Nature Letters*, 439:179–182, January 2006.

[16] R. L. Williams, D. Dalacu, M. E. Reimer, K. Mnaymneh, V. Sazonova, P. J. Poole, G. C. Aers, R. Cheriton, S. Frédérick, D. Kim, J. Lapointe, P. Hawrylak, and M. Korkusinski. Directed self-assembly: a controllable route to optical and electronic devices based on single nanostructures. *Future Trends in Microelectronics: From Nanophotonics to Sensors and Energy*, pages 307–316, 2010.

[17] R. L. Greene, K. K. Bajaj, and D. E. Phelps. Energy levels of wannier excitons in GaAs $\mathrm{Ga}_{1-x}\mathrm{Al}_x\mathrm{As}$ quantum-well structures. *Phys. Rev. B*, 29:1807, 1984.

[18] Y. Arakawa and H. Sakaki. Multidimensional quantum well laser and temperature dependence of its threshold current. *Appl. Phys. Lett.*, 40:939, 1982.

[19] B.F. Levine, C.G. Bethea, G Hasnaina, V.O. Shen, E. Pelve, R.R. Abbott, and S.J. Hsieh. Quantum dots lasers. *Appl. Phys. Lett.*, 56:851–853, February 1990.

[20] D. Atkinson, W.H. Loh, V.V. Afansjev, A.B. Grudinin, A.J. Seeds, and D.N. Payne. Increased amplifier spacing in a soliton system with quantum-well saturable absorbers and spectral filtering. *Optics Lett.*, 19:1514–1516, 1994.

[21] R.B. Laughlin. Anomalous quantum hall effect: An incompressible quantum fluid with factionally charged excitations. *Phys. Rev. Lett.*, 50:1395–1398, 1983.

[22] R.B. Laughlin. Quantized thermal conductance of dielectric quantum wires. *Phys. Rev. Lett.*, 81:232–235, 1998.

[23] Mark Reed. Quantum dots. *Scientific American.*, 268(1):118–123, 1998.

[24] A.P. Alivisatos. Semiconductor clusters, nanocrystals, and quantum dots. *Science*, 16(5251):933–937, 1996.

[25] U. Meirav, M.A. Kastner, and S.J Wind. Single-electron charging and periodic conductance resonances in GaAs nanostructures. *Phys. Rev. Lett.*, 65:771–774, 1990.

[26] B.A. Joyce. Molecular beam epitaxy. *Rep. Prog. Phys.*, 48(1637), 1985.

[27] I. N. Stranski and L. von Krastanov. Abhandlungen der mathematisch-naturwissenschaftlichen klasse. *Akad. Wiss. Lit. Mainz Math.-Naturwiss*, 146:797, 1939.

[28] A. Wojs, P. Hawrylak, S. Fafard, and L. Jacak. Electronic structure and magneto-optics of self-assembled quantum dots. *Phys. Rev. B*, 54:5604, 1996.

[29] H. Hess, E. Betzig, T. Harris, L. Pfeiffer, and K. West. Near field spectroscopy of the quantum constituents of a luminescent system. *Science*, 264:1740, 1994.

[30] L. Landin, M.S. Miller, M.E. Pistol, C.E. Pryor, and L. Samuelson. Optical studies of individual InAs quantum dots in GaAs: Few-particle effects. *Science.*, 280(5361):262, 1998.

[31] U. Bockelmann and W. Heller. Microphotoluminescence studies of single quantum dot. 1. time-resolved experiments. *Phys. Rev. B.*, 55:4456–4468, 1997.

[32] M. Grundmann, O. Stier, and D. Bimberg. InAs/GaAs pyramidal quantum dots: Strain distribution, optical phonons, and electronic structure. *Phys. Rev. B*, 52:11969–11981, 1995.

[33] H. Benisty, C. M. Sotomayor-Torrés, and C. Weisbuch. Intrinsic mechanism for the poor luminescence properties of quantum-box systems. *Phys. Rev. B*, 44(10945), 1991.

[34] T. Inoshita and H. Sakaki. Electron relaxation in a quantum dot: Significance of multiphonon processes. *Phys. Rev. B*, 46(7260), 1992.

[35] J. J. Finley, D. J. Mowbray, M. S. Skolnick, A. D. Ashmore, C. Baker, A. F. G. Monte, and M. Hopkinson. Fine structure of charged and neutral excitons in InAs/$Al_{0.6}$ $Ga_{0.4}$As quantum dots. *Phys. Rev. B*, 66:153316, 2002.

[36] M. Bayer, G. Ortner, O. Stern, A. Kuther, A. A. Gorbunov, A. Forchel, P. Hawrylak, S. Fafard, K. Hinzer, T. L. Reinecke, S. N. Walck, J. P. Reithmaier, F. Klopf, and F. Schafer. Fine structure of neutral and charged excitons in self-assembled In(Ga)As/(Al)GaAs quantum dots. *Phys. Rev. B*, 65:195315, 2002.

[37] S. Raymond, S. Studenikin, A. Sachrajda, Z. Wasilewski, S. J. Cheng, P. Hawrylak W. Sheng, A. Babinski, M. Potemski, G. Ortner, and M. Bayer. Excitonic energy shell structure of self-assembled InGaAs/GaAs dots. *Phys. Rev. Lett.*, 92:187402, 2004.

[38] R.P. Mirin, J.P. Ibbetson, K. Nishi, A.C.Gossard, and J.E. Bowers. 1.3μm photoluminescence from InGaAs quantum dots on GaAs. *Appl. Phys. Lett.*, 67(3795), 1995.

[39] R. Notzel, J. Temmyo, A. Kozen, T. Tamamura, T. Fukui, and H. Hasegawa. Self-organization of strained GaInAs microstructures on InP (311) substrates grown by metalorganic vapor-phase epitaxy. *Laser and Photonics Reviews*, 66(2525), 2009.

[40] T. Miya, Y. Terunuma, T. Hosaka, and T. Miyashita. Ultimate low-loss single-mode fibre at 1.55μm. *Electronics Letters*, 15:106–108, 1979.

[41] K. Nagayama, M. Kakui, M. Matsui, I. Saitoh, and Y. Chigusa. Ultra-low-loss (0.1484 db/km) pure silica core fibre and extension of transmission distance. *Electronics Letters*, 38:1168–1169, 2002.

[42] J.-Y. Marzin, J.-M. Gerard, A. Izrael, D. Barrier, and G. Bastard. Photoluminescence of single InAs quantum dots obtained by self-organized growth on GaAs. *Phys. Rev. Lett.*, 73:716, 1994.

[43] K. Brunner, U. Bockelmann, G. Abstreiter, M. Walther, G. Bóhm, G. Tránkle, and G. Weimann. Photoluminescence from a single GaAs/AlGaAs quantum dot. *Phys. Rev. Lett.*, 69:3216, 1992.

[44] K. Nagayama, M. Kakui, M. Matsui, T. Saitoh, and Y. Chigusa. Ultra-low-loss (0.1484 db/km) pure silica core fibre and extension of transmission distance. *Electronics Letters*, 38(20):1168–1169, September 2002.

[45] K. Takemoto, Y. Sakuma, S. Hirose, T. Usuki, and N. Yokoyama. Observation of exciton transition in 1.3-1.55μm band from single InAs/InP quantum dots in mesa structure. *Jpn. J. Appl. Phys.*, 43(3), 2004.

[46] Danny Kim. Dry passivation studies of gaas (110) surfaces by gallium oxide thin films deposited by electron cyclotron resonance plasma reactive molecular beam epitaxy for optoelectronic device applications. Master's thesis, University of Toronto, 2001.

[47] Michael Reimer. *Electrostatic gating of deterministically positioned indium arsenide/indium phosphide quantum dots.* PhD thesis, University of Ottawa, 2009.

[48] Danny Kim. *Deterministic Control of the Quantum Properties of Single InAs Artificial Atoms with InP Nanoscale Architectures.* PhD thesis, University of Toronto, 2004.

[49] W. Sheng and P. Hawrylak. Atomistic theory of electronic and optical properties of InAs/InP self-assembled quantum dots on patterned substrates. *Phys. Rev. B*, 72:035326, 2005.

[50] S. Fafard, Z.R. Wasilewski, C. Ni. Allen, D. Picard, M. Spanner, J. P. McCaffrey, and P.G. Piva. Manipulating the energy levels of semiconductor quantum dots. *Phys. Rev. B*, 59:15368–15373, 1999.

[51] Pawel Hawrylak and Marek Korkusinsk. *Electronic Properties of Self-Assembled Quantum Dots*, pages 25–91. Springer, 2003.

[52] Dan Dalacu, Michael E. Reimer, Simon Frédérick, Danny Kim, Jean Lapointe, Philip J. Poole, Geof C.Aers, Robin L. Williams, W. Ross McKinnon, Marek Korkusinski, and Pawel Hawrylak. Directed self-assembly of single quantum dots for telecommunication wavelength optical devices. *Laser and Photonics Reviews*, 1(1), March 2010.

[53] P. J. Poole, J. McCaffrey, R. L. Williams, J. Lefebvre, and D. Chithrani. Chemical beam epitaxy growth of self-assembled InAs/InP quantum dots. *J. Vac. Sci. Technol. Bs*, 19(4):1467–1470, 2001.

[54] J. Lefebvre, P. J. Poole, G. C. Aers, D. Chithrani, and R. L. Williams. Tunable emission from InAs quantum dots on InP nanotemplates. *J. of Vac. Sci. and Tech.*, 20(5):2173–2176, September 2002.

[55] D. Gammon, E. S. Snow, B. V. Shanabrook, D. S. Katzer, and D. Park. Fine structure splitting in the optical spectra of single GaAs quantum dots. *Phys. Rev. Lett.*, 76(3005), 1996.

[56] N. Akopian, N. H. Lindner, E. Poem, J. Avron Y. Berlatzky, D. Gershoni, B. D. Gerardot, and P. M. Petroff. Entangled photon pairs from semiconductor quantum dots. *Phys. Rev. Lett.*, 96:130501, 2006.

[57] M. E. Reimer, M. Korkusinski, J. Lefebvre, J. Lapointe, P. J. Poole, G. C. Aers, D. Dalacu, W. R. McKinnon, S. Frédérick, P. Hawrylak, and R. L. Williams. Voltage Induced Hidden Symmetry and Photon Entanglement Generation in a Single, Site-Selected Quantum Dot. *ArXiv e-prints*, June 2007.

[58] Marek Korkusinski, Michael E. Reimer, Robin L. Williams, and Pawel Hawrylak. Engineering photon cascades from multiexciton complexes in a self-assembled quantum dot by a lateral electric field. *Phys. Rev. B.*, 79:035309, 2009.

[59] B. Urbaszek, E.J. McGhee, J.M. Smith, R.J. Warburton, K. Karrai, B.D. Gerardot, J.M. Garcia, and P.M. Petroff. Charged excitons in individual quantum dots: effects of vertical electric fields and optical pump power. *Physica E*, 17:35–36, 2003.

[60] R.J Warbuton, C.S. Durr, K. Karrai, J.P. Kotthaus, G. Medeiros-Ribeiro, and P.M. Petroff. Charged excitons in self-assembled semiconductor quantum dots. *Physical Review Letters*, 79(26), 1997.

[61] B.D. Geradot, S. Seidl, P.A. Dalgarno, R.J Warbuton, D. Granados, J.M. Garcia, K. Karrai, K. Kowalik, O. Krebs, A. Badolato, and P.M. Petroff. Manipulating exciton fine structure in quantum dots with a lateral electric field. *Applied Physics Letters*, 90(041101), 2007.

[62] A. Greilich, M. Schwab, T. Berstermann, T. Auer, R. Oulton, D. R. Yakovlev, and M. Bayer. Tailored quantum dots for entangled photon pair creation. *Phys. Rev. B.*, 73(04532), 2006.

[63] G. Sallen, B. Urbaszek, M. M. Glazov, E. L. Ivchenko, T. Kuroda, T. Mano, S. Kunz, M. Abbarchi, K. Sakoda, D. Lagarde, A. Balocchi, X. Marie, and T. Amand. Dark-bright mixing of interband transitions in symmetric semiconductor quantum dots. *Phys. Rev. Lett.*, 107(166604), October 2011.

[64] Eugene Kadantsev and Pawel Hawrylak. Theory of exciton fine structure in semiconductor quantum dots: Quantum dot anisotropy and lateral electric field. *Phys. Rev. B.*, 81(045311), October 2010.

[65] M. E. Reimer, D. Dalacu, J. Lapointe, P. J. Poole, D. Kim, G. C. Aers, W. R. McKinnon, and R. L. Williams. Single electron charging in deterministically positioned InAs/InP quantum dots. *Appl. Phys. Lett.*, 94:011108, 2009.

[66] S. Raymond, S. Studenikin, S. Cheng, M. Pioro-Ladriere, M. Ciorga, P. Poole, and M. Robertson. Families of islands in InAs/InP self-assembled quantum dots: a census obtained from magneto-photoluminescence. *Semicond. Sci. Technol.*., 18:389–389, 2003.

[67] Danny Kim, Weidong Sheng, Philip J. Poole, Dan Dalacu, Jacques Lefebvre, Jean Lapointe, Michael E. Reimer, Geoff C. Aers, , and Robin L. Williams. Tuning the exciton g-factor in single InAs/InP quantum dots. *Phys. Rev. B.*, 79:045310, 2009.

[68] N.A.J. M. Kleemans, L. van Bree, M. Bozkurt, P.J. van Veldhoven, P.A. Nouwens, R. Notzel, A. Yu. Silov, and P.M. Koenraad. Size-dependent exciton g-factor in self-assembled InAs/InP quantum dots. *Physical Review B*, 79(045311), January 2009.

[69] S. N. Walck and T. L. Reinecke. Exciton diamagnetic shift in semiconductor nanostructures. *Phys. Rev. B*, 57:9088, 1998.

[70] Y. Toda, S. Shinomori, K. Suzuki, and Y. Arakawa. Polarized photoluminescence spectroscopy of single self-assembled InAs quantum dots. *Phys. Rev. B.*, 58:R10147, 1998.

[71] D. Dalacu, S. Frédérick, A. Bogdanov, P. J. Poole, G. C. Aers, and R. L. Willliams. Fabrication and optical characterization of hexagonal photonic crystal microcavities in InP-based membranes containing InAs/InP quantum dots. *J. Appl. Phys.*, 98:023101, 2008.

[72] D. Dalacu, S. Frédérick, P. J. Poole, G. C. Aers, and R. L. Willliams. Postfabrication fine-tuning of photonic crystal microcavities in InAs/InP quantum dot membranes. *Appl. Phys. Lett.*, 87:151107, 2005.